The Hong Kong Polytechnic University

Department of Electronic and Information Engineering

External Magnetic Field Effect on BCC Iron at Elevated Temperatures by Spin-Lattice Dynamics Simulation

by

Chui, Chun Pon

A thesis submitted in partial fulfilment of the requirements for the degree of Master of Philosophy

June 2012

CERTIFICATE OF ORIGINALITY

I hereby declare that this thesis is my own work and that, to the best of my knowledge and belief, it reproduces no material previously published or written, nor material that has been accepted for the award of any other degree or diploma, except where due acknowledgement has been made in the text.

_____ (Signed)

_____CHUI, Chun Pon _____ (Name of student)

Dedication

First, I dedicate the thesis to my parents, who have suffered from my excessive obstinacy in academic pursuit for years. Second, I dedicate the thesis to my deceased aunt, who is too late to witness every progress in the course of my graduate study. Finally, I dedicate the thesis to my friend, Chano, whose soul will stand by me in overcoming my future challenges.

Abstract

The thesis investigates the thermomechanical properties of ferromagnetic body-centered cubic iron under various external magnetic field strengths, using spin-lattice dynamics (SLD) simulations implemented with graphics processing units, emphasizing the external field effect on the magnetic phase transition around the transition temperature regime. Simulation results are presented in terms of ensemble averages of thermodynamic quantities and their derivatives, together with the spectra derived from lattice and spin motions. Then, three major perspectives are sought to analyze the external field effect: classical spins, magnons, and spin-lattice coupling. From the analysis of classical spins, the simulation results show that an external field can reinforce the long range magnetic ordering reflected by the atomic magnetization, and can increase the magnetic phase transition temperature. In addition, the application of an external field allows the SLD magnetization to emulate the mean field magnetization because spin precession modeled by SLD is then suppressed. According to the magnon analysis, an external field inhibits magnon-magnon interaction and maintains the spin stiffness, whose effects are more discernible around the transition temperature regime. Finally, an external field has an insignificant effect on spin-lattice coupling, originated from the more harmonic interatomic potential adopted in our simulations, which cannot reproduce the structural phase-transition from BCC to FCC at 1183K, thus showing stiff lattice vibration. However, both the variation of transition temperature and the magneto-volume effect are observed more prominently around the critical region. As a result, it

can be said classically that an external magnetic field varies the separation dependence of the interatomic potential, which leads to the reduction of the atomic volume. Alternatively in quantum physics, an external field alters the atomic volume because it alters the magnon-magnon interaction, bringing about the change in phonon scattering by phonon-magnon interaction. In short, SLD can model the magneto-volume effect of ferromagnetic materials under an external field, and can help to estimate the resulting transition temperature due to the increased magnetic ordering and inhibited magnon-magnon interaction.

Acknowledgements

I must not hesitate to express my gratitude to Prof. C. H. Woo, my Chief Supervisor. It is he who brings me to the realm of scientific research, and who acts as my role model as a scientific worker. I must thank for his prolonged guidance in my study; his advices have been helpful. I have also learned from him the attitude one should have in academia as well as in life – meticulousness, perseverance, and empathy.

I deeply appreciate Mr. Haohua Wen for his continual support on my thesis, intellectual and spiritual. His scientific mindset, revealed by his remarks, inspires me a great deal. It is certainly much harder to complete my thesis without his support.

It is my pleasure to credit Dr. Pui-Wai Ma for his aid at the start of my graduate study. He was eager to teach me statistical physics and molecular dynamics from scratch, and did not mind that I was ignorant of them. He also provided the core of the simulation program used in the thesis, from which I have recognized many interesting physical phenomena.

Finally, I am indebted to many of my friends for their heartfelt encouragement, especially Mr. H. S. Fok, who is now pursuing an overseas graduate degree. His optimism leads me to tackle difficulties bravely. I wish him success in his forthcoming research career.

Table of Contents

List of Figures

List of Tables

Blank Page

Chapter 1: Introduction

1.1 Motivation

Magnetic materials are playing an increasingly important role in modern industry. Magnetic data storage requires magnetic materials to control the bit to save. Electric machinery requires magnetic materials to control its output power, and the list goes on. In addition to their use in room temperature environment, materials in the magnetic phase, such as ferritic steels, are also employed as structural materials in high temperature environment, such as nuclear fusion and fission reactors, because of their ability to stand damage due to neutron bombardment. Yet, phase changes lead to drastic changes of their physical properties and adversely affect the applicability of their designed function.

Magnetic materials are characterized by the magnetic phase transition across the ferro/paramagnetic (FM/PM) phase boundary, which defines the transition temperature. The transition temperature is determined by the thermal excitations of the spin and lattice subsystems in terms of spin and lattice waves and the associated interaction. Physically, the interaction between the two systems comes from the quantum exchange interaction that couples the electron spins of neighboring atoms. Accordingly, changes in the spin subsystem affect the lattice subsystem, leading to changes of the lattice properties.

The behavior of thermomechanical properties of ferromagnetic iron under an external applied magnetic field is an interesting subject, both in terms of its scientific merit and technical use. We are particularly interested in the

temperature regime around the transition temperature. Investigations of this type can be carried out using the lately developed Spin-Lattice dynamics (SLD) simulation [1],[2], which is what we shall attempt in this thesis.

1.2 Nature of Electron Spin

Magnetism in materials comes from the electron spin. The spin of an atom of a transition metal originates from the electrons of the incomplete *d*-shells, in which a maximum magnetic moment is established according to the Hund's rule. Given an isolated iron atom as an example, 6 *d*-electrons has to be put in a *d*-shell of 5 *d*-electronic orbitals with 10 spin-polarized electronic states. By Pauli's exclusive principle, 5 of the 6 *d*-electrons are put in each *d*-orbital with an up-spin, and the remaining one in a *d*-orbital with a down-spin. Since each electron has a magnetic moment of $1\mu_B$, where μ_B is the Bohr magneton, the net magnetic moment of an isolated iron atom is $4\mu_B$ after cancelling up and down spin states in one of the orbitals. However, the atoms in a crystalline iron solid has a magnetic moment of just $2.2\mu_B$, as a result of the exchange coupling between intra-atomic *d*-electrons and the hybridization between 3*d* and 4*s* electrons.

In a spin-polarized solid, atomic spins interact quantum mechanically via the exchange correlation effect, which is associated with the overlap of the electronic wave-functions. Readers may refer to texts about condensed matter physics, such as the one by Blundell [3], for a better understanding of this topic.

Suppose there are two atoms, each with one electron. While the atomic spacing is sufficiently close, the overlap of the electronic orbitals forces the electrons in these two atoms to stay in the same orbital with opposite spin directions, according to Pauli's exclusion principle. In this case, the material is non-magnetic macroscopically, as shown in Fig. 1.1 as a schematic diagram.

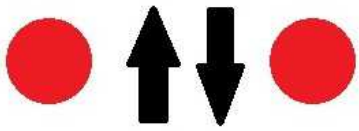

Fig. 1.1 – Spin alignment (black arrows) in anti-parallel configuration when two atoms (red dots) get close to each other.

On the other hand, if the same atoms are put farther away from each other, the electrons would keep a larger distance to minimize electron-electron repulsion. Since the two electrons no longer stay at the same orbital, their spins simply align in parallel to achieve the lowest energy. A material is ferromagnetic if the spins are parallel, and long range magnetic order is established. Fig. 1.2 illustrates this condition schematically.

Fig. 1.2 – Spin alignment (black arrows) in parallel configuration when two atoms (red dots) are far apart.

The spins interact via the exchange interaction as described by the Heisenberg Hamiltonian:

$$H = -\frac{1}{2}\sum_{i \neq j} J_{ij} \boldsymbol{S}_i \cdot \boldsymbol{S}_j \,, \tag{1.1}$$

where J_{ij} is the exchange integral and $\boldsymbol{S}_i$ is the spin of atom i , whose magnitude is determined by the magnetic moment $M_i = g\mu_{\mathrm{B}} S_i$, where $g = 2.0023$ is the electronic *g*-factor. It is noted that the direction M_i is opposite to that of S_i. All spins would align in parallel at the ground state, but thermal fluctuation would disrupt the spin orientation to depart from perfect alignment, so that $M_i(T) < M(0) = 2.2\mu_{\mathrm{B}}$. Further thermal fluctuation due to an increasing temperature can completely destroy the long range magnetic ordering, and the FM/PM phase transition occurs. Conversely, an applied magnetic field forces the atomic spins to align in the same direction and opposes the randomness due to thermal fluctuation. Accordingly, the magnetic moment is a function of temperature and external field strength.

1.3 Magnetic Effect due to External Field

Once an external field $\boldsymbol{H}^{\mathrm{ext}}$ is applied on a magnetic material, spin alignment is enhanced leading to a larger magnetization. Also, the energy contribution by magnetism includes one more term due to the external field, with a value of $g\mu_{\mathrm{B}} \boldsymbol{H}^{\mathrm{ext}} \cdot \sum_i \boldsymbol{S}_i$. Many authors have investigated the effect of the external field on the magnetic phase transition and structural transformation. Thus, Holsten and Primakoff [4] formulated the Hamiltonian of a ferromagnetic

material in domain scale by considering the exchange interaction between magnetic atoms. Wojtowicz and Rayl [5] provided a mean-field analysis of the external field dependence of magnetization and heat capacity in a toroid of cubic, isotropic and ferromagnetic materials, from which an increase of the transition point with the applied field was deduced. Choi *et al.* [6] applied the mean field theory and the field-induced magnetization of iron under a field of decades of Tesla, and then confirmed the increase in temperature of the austenite/ferrite phase transition when an applied magnetic field exists. Koch [7] reviewed that the phase transition temperature of Iron-based alloys between the FCC and BCC phases is a few Kelvins per Tesla of field strength applied. He also suggested that the application of an external field helps to control the desired structure of a material.

1.4 Spin-Lattice Coupling

It can be inferred from the Heisenberg exchange Hamiltonian that the strength of the distance-dependent exchange interaction $J_{ij}\left(\boldsymbol{R}_{ij}\right)$, determined by the degree of atomic orbital overlap, determines the spin stiffness that dictates the collective vibration of the spins, the Curie temperature, and the dynamics of the spin system. In fact, it also determines the lattice dynamics through spin correlation $\boldsymbol{S}_i \cdot \boldsymbol{S}_j$ using the exchange integral, leading to the coupling of spin and lattice subsystems, from which the free energies required for atomic processes would carry contributions from spin system as well as from spin-lattice coupling, especially near the FM/PM transition.

Through the years, researchers have strived to incorporate the effect of spins on the lattice degrees of freedom by diverse approaches, so that a dynamic system of particles can reflect magnetic behavior, especially at the FM/PM phase boundary. For example, Antropov *et al.* [8] attempted to model both spins and lattices by using *ab initio* molecular dynamics and spin dynamics based on the local spin density approximation (LSDA). Stokes *et al.* [9] improved the model of Antropov *et al.* [8], which is restricted to ground states, by introducing non-collinear spin states using the constrained local moment (CLM) method. Körmann *et al.* [10] calculated the vibrational, electronic, and magnetic free energy separately, with the first and second one found by finite-temperature density-functional theory (DFT) under quasi-harmonic approximation, and the third one by many-body Heisenberg Hamiltonian in the mean-field approximation. Sandoval *et al.* [11] investigated phonon softening during the Bain transformation by using the Meyer-Entel potential generated by the embedded-atom method, in which both effects of electronic density and effective charges are considered, yet no magnon contribution is included explicitly in this potential. To further study the same transformation, Okatov *et al.* [12] adopted the projected augmented waves (PAW) and the generalized gradient approximation (GGA) in the electronic density functional, together with the spin spirals (SS) model to represent the varying magnetic order, and with the disordered local moments (DLM) method to describe paramagnetic states of spins, respectively. To model the same transformation, Lavrentiev *et al.* [13] attempted the magnetic-cluster-expansion (MCE) model, whose Hamiltonian includes non-magnetic interaction parameters up to the second nearest neighbors and magnetic interaction parameters up to the fifth nearest neighbors, all of

which are obtained by fitting to DFT calculations. From the above treatments, it is noted that explicit magnon contributions are either contained separately from the lattice subsystem or simply not existent, meaning that real spin-lattice coupling has not yet been modeled at elevated temperatures.

Spin-lattice coupling under a magnetic field was also studied. Matthews and LeCraw [14] measured the magneto-elastic coupling constant in single-crystal yttrium iron garnet by pulse-echo method, and deduced that magnon-phonon interaction was responsible for this coupling. Pomerantz [15] succeeded in exciting spin waves by using microwave phonons with the same frequency.

To achieve real coupling of spin and lattice degrees of freedom in atomistic simulation, Ma, Dudarev and Woo (MWD) [16] developed the spin-lattice dynamics (SLD) simulation scheme, whose main idea is the distance-dependent exchange interaction through which lattice subsystem bridges the spin counterpart. Indeed, the notion of the distance-dependent exchange interaction is confirmed by Wang *et al.* [17], who suggested a complex functional form of the exchange interaction determined by the pair orientation of spins resulting from many-body effects instead of from pairwise contribution. With SLD, the magnetic effects of materials can be modeled to investigate phonon-magnon interaction with temperature, especially at the boundary of magnetic phase transition. This method is also useful for analyzing the free energy of ferromagnetic materials, which is believed to be dependent on the proper treatment of spin-lattice coupling, particularly across the magnetic phase boundary.

One consequence of spin-lattice coupling is the magneto-volume effect, which is the structural deformation, isotropic or anisotropic, in response to the change of magnetization followed by spontaneous or forced magnetic phase transition due to the effect from electrons through phonon-magnon interaction [18]. In fact, according to Takahashi and Shimizu [19], it is the thermodynamic relations obtained by minimizing the free energy F in terms of the number of electrons N, the total magnetic moment M, and the volume V, i.e.,

$$\begin{cases} \dfrac{\partial F(N,M,V)}{\partial M} = 0 \\ \dfrac{\partial F(N,M,V)}{\partial V} = 0 \end{cases} \tag{1.2}$$

that determine the equilibrium configuration arising from the magneto-volume effect. Disordered invar alloy such as the quenched FCC $Fe_{65}Ni_{35}$ [20] is an application of this effect because its thermal expansion coefficient is nearly zero in a certain temperature range due to phonon scattering magnetic excitations.

Many research workers support the notion of spin-lattice coupling leading to the effect. Donaldson [21] suggests that the exchange interaction depends on the material volume that further alters the dependence of temperature on both the magnetic order and the specific heat, despite his claim that his derivation is just useful at or below the Curie temperature. Tanji [22] claimed experimentally that it is the change of the magnetic exchange force, or the derivative of the exchange interaction with respect to interatomic distance, $\mathrm{d}J/\mathrm{d}r$, that leads to the anomalous volume behavior. Oomi and Mōri [23] conducted an experiment to understand the effect in invar alloys under high pressure, which can induce a

change in magnetization, but have not mentioned sufficiently the effect at the magnetic phase transition. Mikhailov and Kazantsev [24] conducted a neutron scattering experiment to show that low-energy magnetic excitation in the form of longitudinal spin fluctuations affects the magneto-volume effect.

In summary, it can be seen from the foregoing discussion that magnetic and mechanical effects at elevated temperatures, resulting from an external magnetic field, is not completely understood. The accompanying magneto-volume effect also needs studying at the atomistic level. More is expected to be done to understand the contribution of an external magnetic field on both spin and lattice properties in ferromagnetic materials, and to investigate the effect originated from an external magnetic field, especially by atomic simulation approach that considers spin-lattice coupling.

1.5 Objective

Based on the shortcomings in the existing work on the effect on the external magnetic field, the thesis adopts the SLD simulation to study the effects of external field on magnetic ordering in BCC iron at elevated temperatures. In addition, the temperature dependence of magneto-volumetric effect is also investigated.

The thesis is organized as follows. Chapter 2 provides a preliminary discussion of statistical thermodynamics, as the basis to analyze the forthcoming computer experiment results. It also mentions spin-lattice dynamics as a tool to investigate atomic behavior under a magnetic field. This chapter finally illustrates the necessity and implementation of a computer system relying on

graphics processing units when one wants to solve molecular-level problems. Chapter 3 describes the methodology of the study. It begins with the simulation settings for the study, followed by collection and analysis of data for interpretation. The final section of this chapter explains the method of finding data averages, phonon and magnon spectra, and derivatives of observables. Chapter 4 discusses the temperature dependence of magnetic ordering realized by SLD simulation. This issue is analyzed by magnetization, spin correlation coefficients, spin temperature, and magnon spectra. Many of them can demonstrate the change of the transition temperature in the presence of an applied field. It also discusses the effect of spin-lattice coupling, which can be observed by the magneto-volume effect, by means of an analysis of the resulting volume change. It can be regarded that it is the compromise between the temperature and the external field strength that determines the equilibrium volume of a piece of ferromagnetic material. Chapter 5 is the summary and conclusion of the thesis.

1.6 References

[1] P.-W. Ma, C. H. Woo, and S. L. Dudarev, Phys. Rev. B **78**, 024434 (2008).

[2] P.-W. Ma, S. L. Dudarev, A. A. Semenov, and C. H. Woo, Phys. Rev. E **82**, 031111 (2010).

[3] S. Blundell, *Magnetism in Condensed Matter* (Oxford University Press, New York, 2001).

[4] T. Holsten and H. Primakoff, Phys. Rev. **58**, 1098 (1940).

[5] P. J. Wojtowicz and M. Rayl, Phys. Rev. Lett. **20**, 1489 (1968).

[6] J. K. Choi, H. Ohtsuka, Y. Xu, and W. Y. Choo, Scripta Mater. **43**, 221 (2000).

[7] C. C. Koch, Mater. Sci. Eng. A **287**, 213 (2000).

[8] V. P. Antropov, M. I. Katsnelson, M. van Schilfgaarde, and B. N. Harmon, Phys. Rev. Lett. **75**, 729 (1995).

[9] G. M. Stocks, B. Ujfalussy, X. Wang, D. M. C. Nicholson, W. A. Shelton, Y. Wang, A. Canning, and B. L. Györffy, Phil. Mag. B **78**, 665 (1998).

[10] F. Körmann, A. Dick, B. Grabowski, B. Hallstedt, T. Hickel, and J. Neugebauer, Phys. Rev. B **78**, 033102 (2008).

[11] L. Sandoval, H. M. Urbassek, and P. Entel, Phys. Rev. B **80**, 214108 (2009).

[12] S. V. Okatov, A. R. Kuznetsov, Y. N. Gornostyrev, V. N. Urtsev, and M. I. Katsnelson, Phys. Rev. B **79**, 094111 (2009).

[13] M. Y. Lavrentiev, D. Nguyen-Manh, and S. L. Dudarev, Phys. Rev. B **81**, 184202 (2010).

[14] H. Matthews and R. C. LeCraw, Phys. Rev. Lett. **8**, 397 (1962).

[15] M. Pomerantz, Phys. Rev. Lett. **7**, 312 (1961).

[16] P.-W. Ma, C. H. Woo, and S. L. Dudarev, Phys. Rev. B **78**, 024434 (2008).

[17] H. Wang, P.-W. Ma, and C. H. Woo, Phys. Rev. B **82**, 144304 (2010).

[18] D. J. Kim, Phys. Rev. B **39**, 6844 (1989).

[19] I. Takahashi and M. Shimizu, J. Phys. F: Met. Phys. **18**, 2081 (1988).

[20] B. Grossmann and D. G. Rancourt, Phys. Rev. B **54**, 12294 (1996).

[21] R. H. Donaldson, Phys. Rev. **157**, 366 (1967).

[22] Y. Tanji, J. Phys. Soc. Jpn. **31**, 1366 (1971).

[23] G. Oomi and N. Mōri, Physica B **119**, 149 (1983).

[24] Y. N. Mikhailov and V. A. Kazantsev, Phys. Met. Metallogr. **97**, 25 (2004).

Chapter 2: Background Knowledge

2.1 Thermodynamics Quantities

1. Statistical Thermodynamics

Classical thermodynamics studies macroscopic thermodynamic quantities in equilibrium states via the laws that govern their behavior and the relations among them, without the linkage to their microscopic atomistic origin. Through the brilliant works of Boltzmann, Einstein, Gibbs, and many others, statistics was found to be able to provide the missing link between the macroscopic thermodynamics properties and microscopic atomistic information. Interested readers may refer to texts such as the ones by Mandl [1] and Reif [2] for a preliminary understanding of this topic. In this thesis, statistical thermodynamics will be the basis of our methodology, through which we obtain the thermo-mechanical properties of a ferromagnetic metal from the dynamics of the spin and lattice degrees of freedom of the atoms obtained from atomistic simulations.

A microstate of a system of particles is a specific state defined by the particle conditions and controlled by their probability of occurrences. Within the phase space concept, each microstate is represented by a point in the phase space of nN dimensions, constituted by N particles each having n degrees of freedom. For example, in an Einstein solid with N atoms vibrating as N independent harmonic oscillators with a unique frequency, the phase space has $6N$ dimensions, and each oscillator is described by the 6 degrees of freedom of

its position $\boldsymbol{r}_i$ and momentum $\boldsymbol{p}_i$. A microstate is then regarded as a point $s=\left(\{\boldsymbol{r}_i\},\{\boldsymbol{p}_i\}\right)$ in the phase space determined by the position space $\{\boldsymbol{r}_i\}$ and momentum space $\{\boldsymbol{p}_i\}$. The time series of the phase space points is called the phase trajectory $\Gamma\left(\{\boldsymbol{r}_i\},\{\boldsymbol{p}_i\}\right)$.

In contrast, a macrostate is a set of all the microstates representing a particular probability of occurrences. A statistical ensemble is the set of microstates that belong to the same macrostate, such as with the same volume and energy. It can be regarded as a collection of the phase-space points belonging to a given macrostate.

Observables are used as a general description of all atoms, implemented by ensemble averaging. Suppose that a physical quantity has a certain probability distribution $P\left(\{\boldsymbol{r}_i\},\{\boldsymbol{p}_i\}\right)$. The ensemble average of an observable A is defined using the distribution as

$$\left\langle A\left(\{\boldsymbol{r}_i\},\{\boldsymbol{p}_i\}\right)\right\rangle_{\text{ensemble}}=\frac{\int \mathrm{d}^N\boldsymbol{r}_i\int \mathrm{d}^N\boldsymbol{p}_i A\left(\{\boldsymbol{r}_i\},\{\boldsymbol{p}_i\}\right)P\left(\{\boldsymbol{r}_i\},\{\boldsymbol{p}_i\}\right)}{\int \mathrm{d}^N\boldsymbol{r}_i\int \mathrm{d}^N\boldsymbol{p}_i P\left(\{\boldsymbol{r}_i\},\{\boldsymbol{p}_i\}\right)}. \qquad (2.1)$$

However, if the system is ergodic, i.e. if every possible phase space coordinate is accessible as is assumed in atomistic simulations, the ensemble average is equal to the time average, i.e.,

$$\left\langle A\left(\{\boldsymbol{r}_i\},\{\boldsymbol{p}_i\}\right)\right\rangle_{\text{time}}=\lim_{t_{\text{obs}}\to\infty}\frac{1}{t_{\text{obs}}}\int_0^{t_{\text{obs}}}A\left(\{\boldsymbol{r}_i\},\{\boldsymbol{p}_i\}\right)\mathrm{d}t, \qquad (2.2)$$

with t_{obs} being the time period of observation. In fact, time averages are often used in molecular simulations to evaluate an observable.

Two common ensembles are available, *NVE* and *NVT* ensembles. If the system has a fixed number of atoms N at constant volume V and constant energy E, a microcanonical (*NVE*) ensemble is specified. This ensemble is isolated since it does not allow material or energy exchange with the surroundings. Statistical thermodynamics assumes that each microstate has an equal *a priori* probability, which means that every microstate is equally likely to occur. Therefore, the probability of occurrence of a macrostate depends on the statistical weight $\Omega(N,V,E)$, which is the number of microstates in that macrostate. In statistical thermodynamics, the largest probability of occurrence belongs to the equilibrium state having the largest statistical weight. The entropy S of the *NVE* ensemble is defined as

$$S(N,V,E) = k_B \ln \Omega(N,V,E), \tag{2.3}$$

where k_B is the Boltzmann constant. From this definition, maximum entropy occurs at equilibrium with the largest number of microstates. From the foregoing, the linkage between the microscopic and macroscopic behaviors of a system is established.

When a system interacts with its environment, energy and momentum exchange occurs. In thermal equilibrium the system attains the same temperature and/or pressure as its environment. Such a system is called a canonical ensemble, in which the number of atoms *N,* the volume *V* and the temperature *T* are kept

fixed and are well-defined quantities, but not its total energy E. In a canonical ensemble, the probability P_i of a macrostate with energy E_i obeys the Boltzmann distribution, i.e.

$$P_i = e^{-\beta E_i} / Z \,, \tag{2.4}$$

where $\beta = 1/k_{\mathrm{B}}T$ is the temperature parameter, with k_{B} being the Boltzmann constant, and Z is so-called the partition function,

$$Z = \sum_i e^{-\beta E_i} \,, \tag{2.5}$$

which can be treated as the normalized factor, such that $\sum_i P_i = 1$. The entropy is given by

$$S = -k_{\mathrm{B}} \sum_i P_i \ln P_i \,, \tag{2.6}$$

which is regarded as a generalization of Eq. (2.3) because the probability of occurrence of a state no longer has to be equally likely.

Due to the heat transfer between the system and its environment, the total energy of a canonical ensemble in thermal equilibrium fluctuates around a specific value, so that the average total energy is usually defined to correspond to the internal energy in thermodynamics, i.e.

$$\bar{E} = \sum_i P_i E_i = \frac{1}{Z} \sum_i e^{-\beta E_i} E_i = -\frac{\partial \ln Z}{\partial \beta} \,. \tag{2.7}$$

2. Vibrational Energy

Energy added to a system of atoms produces excitations in their collective vibratory motion, in the form of additional components from higher-frequency modes. The result is an increase of the energy and temperature of the system. However, the energy supplied to the system does not necessarily all go to excite the atoms, because part of it might have to be expended in doing work in relation to the volume change of the system due to the anharmonicity of restoring forces experienced by atomic displacements.

Indeed, the total energy of the system is the sum of the static energy of the atoms due to the interatomic potential plus the kinetic energy from the atomic vibrations (vibrational energy) E^{vib}. The thermodynamic meaning of these mechanical energies can be understood by referring to the phase diagram in Fig. 2.1, which describes a thermal expansion process under stress-free condition. An infinite number of thermodynamic paths are available to achieve thermal expansion from state A at (T_0, V_0) to state B at (T_1, V_1), where $T_0 < T_1$ and $V_0 < V_1$. Specifically, the curly path in Fig. 2.1 describes the reversible process in which

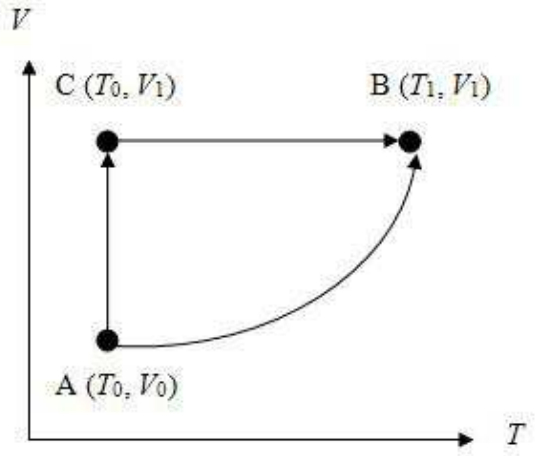

Fig. 2.1 – Phase diagram explaining the definition of vibrational energy. The heat absorbed during process CB is the vibrational energy at constant volume from temperature T_0 to T_1.

both the temperature and volume are simultaneously changed under quasi-equilibrium conditions. The process can be decomposed into two processes as represented in Fig. 2.1, by straight lines AC and CB, respectively, where C is the intermediate state at temperature T_0 and volume V_1. The vertical line AC is the constant-temperature process associated with the work done by the system $W(V_1 - V_0)$ when its volume changes from V_0 to V_1. The horizontal line CB is the constant-volume process associated with the increase of the amount of heat $Q(T_1 - T_0)$ in the system associated with the change in entropy due to the relaxation of microstates when the temperature is raised from T_0 to T_1. Taking (T_0, V_0) as the reference state, the stress-free total energy at temperature T^{eq} and atomic volume V^{eq} can be written as

$$E\left(T^{\text{eq}}, V^{\text{eq}}\right) = Q\left(T^{\text{eq}}\right) + W\left(V^{\text{eq}}\right). \tag{2.8}$$

One may equate the isothermal W to the change in static energy, and the isovolumetric Q with the change in vibrational energy. The specific heat $C_V(T)$ of the system at this state is the temperature gradient of the vibrational energy, rather than the total energy $E\left(T^{\text{eq}}, V^{\text{eq}}\right)$, i.e.,

$$C_V(T) = \left(\frac{\mathrm{d}Q}{\mathrm{d}T}\right)_V = \left(\frac{\partial E^{\text{vib}}}{\partial T}\right)_V. \tag{2.9}$$

2.2 Hamiltonian and Formulations

A ferromagnetic crystal in an external magnetic field is classically regarded as a dynamical system of N atoms with $9N$ degrees of freedom from their instantaneous momenta, positions and spins. The Hamiltonian can be written as [3-4]

$$H = \sum_i \frac{\boldsymbol{p}_i^2}{2m_i} + U\left(\{\boldsymbol{R}\}\right) - \frac{1}{2}\sum_{i,j} J_{ij}\left(\{\boldsymbol{R}\}\right)\boldsymbol{S}_i \cdot \boldsymbol{S}_j + g\mu_{\mathrm{B}}\boldsymbol{H}^{\mathrm{ext}} \cdot \sum_i \boldsymbol{S}_i \qquad (2.10)$$

where $J_{ij}\left(\{\boldsymbol{R}\}\right)$ is the exchange field depending on the atomic position space of the N atoms $\{\boldsymbol{R}\}$. m_i is the mass of atom i, $\boldsymbol{p}_i$ is its momentum and $\boldsymbol{S}_i$ its spin. In this thesis, we assume that $\boldsymbol{S}_i$ has a fixed magnitude corresponding to a magnetic moment of $1.1\mu_{\mathrm{B}}$ (BCC iron). $\boldsymbol{H}^{\mathrm{ext}}$ is the external field, and $U\left(\{\boldsymbol{R}\}\right)$ is the interatomic magnetic potential.

The corresponding equations of motion can be derived from classical mechanics:

$$\frac{\mathrm{d}\boldsymbol{R}_k}{\mathrm{d}t} = \frac{\partial H}{\partial \boldsymbol{p}_k} = \frac{\boldsymbol{p}_k}{m_k}, \qquad (2.11)$$

$$\frac{\mathrm{d}\boldsymbol{p}_k}{\mathrm{d}t} = -\frac{\partial H}{\partial \boldsymbol{R}_k} = -\frac{\partial U\left(\{\boldsymbol{R}\}\right)}{\partial \boldsymbol{R}_k} + \frac{1}{2}\frac{\partial}{\partial \boldsymbol{R}_k}\sum_{i,j} J_{ij}\left(\{\boldsymbol{R}\}\right)\left(\boldsymbol{S}_i \cdot \boldsymbol{S}_j\right), \qquad (2.12)$$

$$\frac{\mathrm{d}\boldsymbol{S}_i}{\mathrm{d}t} = \frac{1}{\hbar}\boldsymbol{S}_i \times g\mu_{\mathrm{B}}\boldsymbol{H}_i^{\mathrm{eff}}. \qquad (2.13)$$

We remind that although the equations of motion is derived classically, spin and spin-spin interaction via the exchange field are all quantum concepts. In Eq. (2.13), $\hbar$ is the reduced Planck constant, and

$$\boldsymbol{H}_i^{\text{eff}} = \frac{1}{g\mu_{\text{B}}} \sum_j J_{ij} \boldsymbol{S}_j - \boldsymbol{H}^{\text{ext}} \tag{2.14}$$

is treated as the effective magnetic field experienced by an atom *i* due to the external field and the internal interaction field by neighboring spins. It is noticed that the equations of motion of momenta and position follow the conventional MD approach. Exchange interaction due to spins is entirely a phenomenon of quantum mechanics, so its equation of motion must be solved quantum mechanically by applying the Poisson Brackets $[\ldots]$ to the Hamiltonian due to spin dynamics

$$H^{\text{spin}} = -\frac{1}{2} \sum_{i,j} J_{ij} \left(\{ \boldsymbol{R} \} \right) \boldsymbol{S}_i \cdot \boldsymbol{S}_j + g\mu_{\text{B}} \boldsymbol{H}^{\text{ext}} \cdot \sum_i \boldsymbol{S}_i \,, \tag{2.15}$$

and obtain the equation of motion of spin in Eq. (2.13), using

$$\frac{\mathrm{d}\boldsymbol{S}_i}{\mathrm{d}t} = \frac{i}{\hbar} \left[H^{\text{spin}}, \boldsymbol{S}_i \right] \tag{2.16}$$

The effect of an external field on spin-lattice coupling can be realized from the equations of motion. According to Eq. (2.13), the external field $\boldsymbol{H}^{\text{ext}}$ changes the norm of the effective magnetic field and the angle between the external field and the spins, in order that the spin motion is altered. The resulting spin vectors

are substituted to Eq. (2.12) to change the particle motion, which further changes the atomic separation found by Eq. (2.11).

2.3 Spin-Lattice Dynamics (SLD)

1. Introduction

Conventional molecular dynamics simulation is based on lattice dynamics, and fails to model magnetic materials due to the dynamical effects of spin-lattice interaction, even with the help of a magnetic potential developed by Chiesa, Derlet and Dudarev [5]. In view of this problem, Ma, Woo and Dudarev [3-4] developed the SLD scheme that treats lattice and spin subsystems on equal footing, which is discussed in this section

2. Hamiltonian and Equations of Motion

The SLD algorithm we used assumes a constant magnitude of the atomic spin, and it just focuses on the spin orientation. Rather than implementing Eq. (2.10), the SLD algorithm simply process the Hamiltonian as

$$H = \sum_i \frac{\boldsymbol{p}_i^2}{2m_i} + U\left(\{\boldsymbol{R}\}\right) - \frac{1}{2}\sum_{i,j} j_{ij}\left(\{\boldsymbol{R}\}\right)\boldsymbol{e}_i \cdot \boldsymbol{e}_j + g\mu_{\mathrm{B}} S\boldsymbol{H}^{\mathrm{ext}} \cdot \sum_i \boldsymbol{e}_i \qquad (2.17)$$

where $j_{ij}\left(\{\boldsymbol{R}\}\right) = J_{ij}\left(\{\boldsymbol{R}\}\right)S^2$ is the exchange integral subsuming the magnitude S of both spins i and j. After the spin magnitudes are absorbed, each spin is now treated as a unit spin vector $\boldsymbol{e}_i$ with 2 spin degrees of freedom, from which the magnetic energy of each atom i due to neighboring spins j is defined. In

SLD, the exchange integral considers the first and second nearest neighbor atoms; effects due to farther atoms are ignored.

The equations of motion used in SLD are then expressed in terms of the unit spin vectors as

$$\frac{\mathrm{d}\boldsymbol{R}_k}{\mathrm{d}t} = \frac{\partial H}{\partial \boldsymbol{p}_k} = \frac{\boldsymbol{p}_k}{m_k}, \tag{2.18}$$

$$\frac{\mathrm{d}\boldsymbol{p}_k}{\mathrm{d}t} = -\frac{\partial H}{\partial \boldsymbol{R}_k} = -\frac{\partial U\left(\{\boldsymbol{R}\}\right)}{\partial \boldsymbol{R}_k} + \frac{1}{2}\frac{\partial}{\partial \boldsymbol{R}_k}\sum_{i,j} j_{ij}\left(\{\boldsymbol{R}\}\right)\left(\boldsymbol{e}_i \cdot \boldsymbol{e}_j\right), \tag{2.19}$$

$$\frac{\mathrm{d}\boldsymbol{e}_i}{\mathrm{d}t} = \frac{1}{\hbar}\boldsymbol{e}_i \times g\mu_{\mathrm{B}} S\boldsymbol{H}_i^{\mathrm{eff}}., \tag{2.20}$$

with

$$\boldsymbol{H}_i^{\mathrm{eff}} = \frac{1}{g\mu_{\mathrm{B}}}\sum_j J_{ij}\boldsymbol{e}_j - \boldsymbol{H}^{\mathrm{ext}} \tag{2.21}$$

3. Integration Algorithm

The phase trajectory is obtained by solving the equations of motion, in which the Suzuki-Trotter decomposition (STD) is used for integrating the position, velocity, and spin velocity operators simultaneously in SLD scheme. Suppose that the generalized coordinate $\boldsymbol{x}$ is related to the Hamiltonian operator $\hat{H}$ in Eq. (2.10) by

$$\frac{d\boldsymbol{x}}{dt} = \hat{H}\boldsymbol{x}\,. \tag{2.22}$$

If we set $\hat{H}\boldsymbol{x} = \left(\hat{P} + \hat{F} + \hat{S}\right)\boldsymbol{x}$, where $\hat{P}$, $\hat{F}$, and $\hat{S}$ are operators resulting the solutions to the momentum, force, and spin orientation, respectively, such that

$$\begin{aligned}
\hat{P}\boldsymbol{x} &\equiv \frac{\boldsymbol{p}}{m} \\
\hat{F}\boldsymbol{x} &\equiv -\frac{\partial U}{\partial \boldsymbol{R}} + \frac{1}{2}\sum_{i,j}\frac{\partial J_{ij}\left(\{\boldsymbol{R}\}\right)}{\partial \boldsymbol{R}}\left(\boldsymbol{e}_i \cdot \boldsymbol{e}_j\right), \\
\hat{S}\boldsymbol{x} &\equiv \boldsymbol{e}\times\left(\frac{1}{g\mu_{\mathrm{B}}}\sum_i J_i \boldsymbol{e}_i - \boldsymbol{H}^{\mathrm{ext}}\right)
\end{aligned} \tag{2.23}$$

then according to the general solution to $\boldsymbol{x}$,

$$\boldsymbol{x}\left(t + \Delta t\right) = e^{\hat{H}\Delta t}\boldsymbol{x}\left(t\right), \tag{2.24}$$

and STD, we have

$$e^{\hat{H}\Delta t}\boldsymbol{x}\left(t\right) = e^{\left(\hat{P}+\hat{F}+\hat{S}\right)\Delta t}\boldsymbol{x}\left(t\right) = e^{\hat{S}(\Delta t/2)}e^{\left(\hat{P}+\hat{F}\right)\Delta t}e^{\hat{S}(\Delta t/2)}\boldsymbol{x}\left(t\right) + O\left(\Delta t^3\right). \tag{2.25}$$

Since motion of a spin depends on neighboring spins, the spin velocity operator can be expressed as the sum of all individual spin operators:

$$\hat{S} = \hat{S}_1 + \hat{S}_2 + \cdots + \hat{S}_{N-1} + \hat{S}_N. \tag{2.26}$$

The spin motion is thus found, according to STD, by

$$\begin{aligned}
e^{\hat{S}\Delta t}\boldsymbol{x}\left(t\right) = {} & e^{\hat{S}_1(\Delta t/2)}e^{\hat{S}_2(\Delta t/2)}\cdots e^{\hat{S}_{N-1}(\Delta t/2)} \\
& \times e^{\hat{S}_N(\Delta t)}e^{\hat{S}_{N-1}(\Delta t/2)}\cdots e^{\hat{S}_2(\Delta t/2)}e^{\hat{S}_1(\Delta t/2)}\boldsymbol{x}\left(t\right) + O\left(\Delta t^3\right).
\end{aligned} \tag{2.27}$$

4. Temperature Control

SLD simulation adopts the Langevin thermostat on the lattice and spin subsystem, governed by the fluctuation-dissipation theorem [6], which is justified for modeling the physical phenomenon of metallic ions and electrons. In essence, the Langevin thermostat models the stochastic nature of atomic motions instead of using the deterministic equations of motion in Eq. (2.18) to Eq. (2.20). In metals, free electrons leave the atoms and move randomly around the positive ions remaining. In this case, the free electrons can be regarded as providing the random forces to the positive ions, which dissipate their energy due to the electron 'viscosity'. Under thermal equilibrium, the exchange of energy by this way is stabilized, and the temperature reaches a constant value. The implementation of Langevin thermostat is to replace the deterministic equation of motion stated in Eqs (2.12) and (2.13) by the Langevin equation. The equation for the lattice subsystem is rewritten as

$$m\frac{\mathrm{d}\boldsymbol{v}}{\mathrm{d}t} = -\frac{\partial \tilde{U}}{\partial \boldsymbol{r}} - \gamma \boldsymbol{v} + \boldsymbol{f}(t), \tag{2.28}$$

where $\boldsymbol{v}$ is the velocity of an atom, and $\tilde{U}$ is the total potential including both lattice and spin contributions. The first term on the right hand side of Eq. (2.28) represents the interatomic force provide by the atomic potential, whereas the second term is the frictional force with coefficient of friction γ, and the third term is the random force $\boldsymbol{f}$ with a delta-correlation,

$$\left\langle \boldsymbol{f}(t) \cdot \boldsymbol{f}(t') \right\rangle = \mu\delta(t - t'). \tag{2.29}$$

Here, μ is the amplitude of this random force. The random force increases the kinetic energy while the frictional force decreases it. However, these two forces would balance finally at a preset temperature when the system reaches a thermodynamic equilibrium state. To find the relation between the coefficient of friction, the random force amplitude, and temperature, one may map Eq. (2.29) into a Fokker-Planck equation. Under thermal equilibrium, as the system follows Gibbs distribution, μ, γ and T should satisfy such a relationship

$$\mu = 6\gamma k_{\mathrm{B}} T . \tag{2.30}$$

The absolute temperature at equilibrium is thus determined. In other words, the friction and fluctuation properties determine the temperature; one simply controls these properties to maintain the desired temperature.

Similarly, for the spin subsystem, the temperature can be controlled within the corresponding Langevin thermostat, where the Langevin equation for spin dynamics is written in the form

$$\frac{\mathrm{d}\boldsymbol{S}_k}{\mathrm{d}t} = \frac{1}{\hbar}\left[\boldsymbol{S}_k \times \left(\boldsymbol{H}_k^{\mathrm{eff}} + \boldsymbol{h}_k\right) - \eta \boldsymbol{S}_k \times \left(\boldsymbol{S}_k \times \boldsymbol{H}_k^{\mathrm{eff}}\right)\right], \tag{2.31}$$

where η is the damping coefficient of friction for dissipation purpose, and $\boldsymbol{h}_k$ is the fluctuation of the effective field $\boldsymbol{H}_k^{\mathrm{eff}}$, which is delta-correlated with random noise amplitude as

$$\left\langle \boldsymbol{h}_i(t') \cdot \boldsymbol{h}_j(t'') \right\rangle = \xi \delta_{ij} \delta(t' - t'') . \tag{2. 32}$$

Here, δ_{ij} is the Kronecker delta. The spin Langevin thermostat bases on the fluctuation-dissipation theorem, and permits the exchange of spin energy and angular momentum with the system. To determine the random noise amplitude, Eq. (2.32) is mapped to the Fokker-Planck equation. In thermal equilibrium of spin subsystem, Gibbs distribution is established, and we map the distribution to the mapped equation to obtain the random noise amplitude as

$$\xi = 2\Pi_k k_B T \eta \,, \tag{2.33}$$

where Π_k is the spin angular momentum.

5. Stress Control

SLD employs the Berendsen barostat [7], which is essentially a pressure bath and the volume is slowly scaled to the desired one with fluctuations of volume being introduced, which improves simple volume scaling. In SLD scheme, the atomic stress experienced by an atom i is derived according to the virial theorem [8] as,

$$\sigma^i_{\alpha\beta} = \frac{1}{V_i}\left(m_i v_\alpha v_\beta + \frac{1}{2}\sum_{i\neq j} f_{ij\alpha} r_{ij\beta} \right), \tag{2.34}$$

where α and β represent Cartesian components, V_i is the atomic volume, v_α and v_β are the velocities, $f_{ij\alpha}$ is the atomic force component between atom i and j along α direction, and $r_{ij\alpha}$ is the atomic separation between atom i and j along α direction. To scale the average atomic stress $\left\langle \sigma^i_{\alpha\alpha} \right\rangle$ to the desired

stress $s_{\alpha\alpha}$ in barostat along α direction, the box size $\{L_\alpha\}$ is multiplied by a factor χ_α at each time step Δt,

$$\begin{cases} L'_\alpha = \chi_\alpha L_\alpha \\ x'_i = \chi_x x_i \\ y'_i = \chi_x y_i \\ z'_i = \chi_x z_i \end{cases}, \tag{2.35}$$

with

$$\chi_\alpha = 1 - \frac{\beta_c}{3}\frac{\Delta t}{t_R}\left(s_{\alpha\alpha} - \left\langle \sigma^i_{\alpha\alpha} \right\rangle\right). \tag{2.36}$$

Here, β_c is the compressibility of the bulk, t_R is the relaxation time characterizing the stabilizing rate of the barostat.

2.4 Parallel Processing and Graphics Processing Units (GPUs)

1. Practical Values of GPUs

Computational power has been a bottleneck of atomistic simulations. For example, early computers for molecular dynamics simulations could only process hundreds of atoms. However, in recent years, larger systems can be implemented in view of the rapid development of computation technology. Novel parallel computation implementations have been breaking the record of processing speed. For example, in 2011, Tianhe-1 supercomputer of China has been capable of computing the interactions between 110 billion atoms simultaneously at 1.87 petaflops. During the period of rapid development, parallel computation can be

regarded as a promising approach due to its utilization of memory dedicated to computation process. In this process, the computing task is speeded up by organizing a big computation problem into a number of threads, which are processed concurrently. The value from each thread is then summed up for the final answer to a problem.

It has to be addressed that large-scale computations in the last decades have been taken part in CPU constrained by the expensive cache memory and by the required sequential processing. Moreover, CPU computation has exhibited its physical limit, as the size of a CPU has already reached the quantum limit. Fortunately, the first GPU developed by NVIDIA in 1999 could tackle the problems in CPU by employing parallel computing capabilities. Together with the GPU-specific parallel programming language CUDA launched in 2006, the true power of parallel computation was realized by worldwide GPU developers.

The advantage of using GPU is that more memory resources are devoted to computations, rather than to the communication between various computation chips. Also, the power efficiency of GPU is superior because such a chip can generate computations of gigaflops per Watt. Accordingly, GPU is employed as a popular tool for atomistic simulations, as is done in the thesis.

In fact, independence for parallel computation can be achieved in SLD by considering partitions of atom groups according to the cut-off distance of spin and lattice interactions, such that each of these groups shows no effect on others [9]. The whole phase space is then changed accordingly at each time step after all

groups are computed concurrently, and parallel computation continues in the next time step.

Readers may consult Kirk and Hwu [10] for the key features of a GPU, which is briefly discussed briefly in Sections 2 and 3 below. Section 4 will demonstrate a method to build a GPU server for computational purposes.

2. Hardware Structure

Because more transistors are devoted to computations in GPU than in a central processing unit (CPU), while those for cache and control units are reduced, GPUs are suitable for parallel computations according to the architecture. This design is advantageous because the enhanced computation power is enough to cover the rise of memory latency due to fewer memory resources. After all, GPU advocates data-parallel processing on each core; communication among the cores by cache and memory is less important.

NVIDIA GPU adopts the Single Instruction Multiple Data (SIMD) architecture. All 8 cores in a multiprocessor perform the same instruction, but calculate on different sets of data. All these 8 cores have attached their own register for processing data quickly, and communicate with each other by the same shared memory in the multiprocessor. All multiprocessors in a GPU chip use the same device memory. Fig. 2.2 shows this architecture schematically.

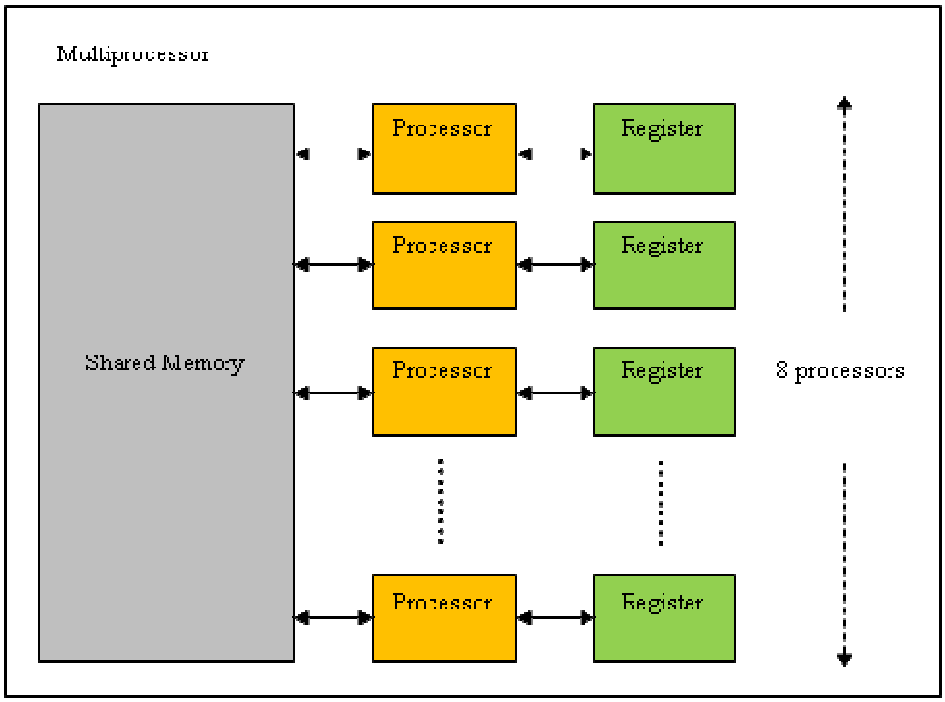

Fig. 2.2 – Key features of hardware configuration in an NVIDIA GPU multiprocessor.

3. Programming Structure

The author will adopt NVIDIA hardware in this thesis, so Compute Unified Device Architecture (or CUDA) is relied on, which is the programming language for such computational hardware units. In this programming architecture, a process is divided into a number of computational groups called threads, and CUDA handles all these threads concurrently to achieve speedup. CUDA is scalable in that thread blocks of a program are allocated to each GPU core automatically. Therefore, the run time for a given program is reduced by using a GPU with more cores.

In CUDA, the heterogeneous programming model is adopted, in which the host (CPU) controls the device (GPU) by means of kernels. In this model, the CPU instructs the GPU to allocate memory for forthcoming data, and commands

the GPU to execute threads concurrently. The CPU then copies the data to the GPU for computation. GPU executes the computation steps and saves the results in GPU memory. Lastly, the CPU would copy the results in the GPU memory to the CPU memory. In this regard, the programmer has to determine the program sections which allow and disallow parallel processing. Those permitting parallel processing go to the GPU, and those forbidding parallel processing go to the CPU. As a reminder, the host accepts C and C++ programming language, while the device accepts CUDA only.

GPU programming involves handling of threads in some predefined order in the programming stage, achieved by defining a number of grids which store a number of independent blocks, each containing at most 1,024 threads [11]. Fig. 2.3 shows the organization of threads allowed in CUDA. In this figure as an example, there is a grid with 4 blocks in *x*-direction and 2 blocks in *y*-direction, respectively. In each of the blocks, there are 4 threads in *x*-direction and 5 threads in *y*-direction, respectively. The programmer just instructs the GPU cores to loop over every thread by traversing every block in every grid and by executing a kernel on each thread. To ensure that all threads in a block have completed a task before continuing further, we may use `__syncthreads()` command in the kernel. In turn, to ensure that changes in the global memory and shared memory are visible to all threads in a grid, we may use `__threadfence()` command in the kernel.

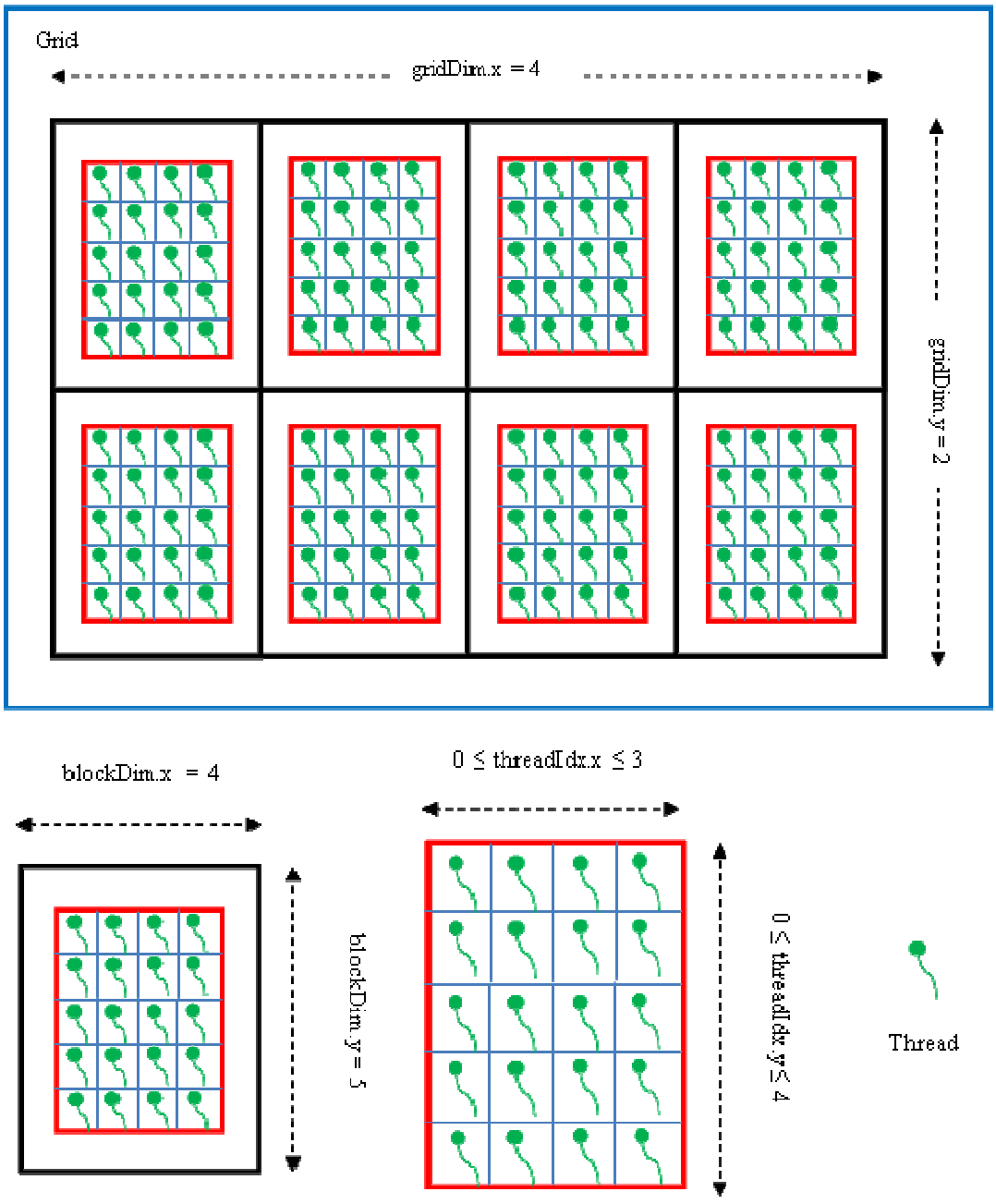

Fig. 2.3 – Thread block organization in a grid.

4. Assembly and Configuration of GPU System

Although dedicated GPU servers are obtainable from many IT solution companies at a prohibitive cost for ordinary people, we can still build a GPU server on our own, according to our budget and needs. This section describes the way of building a GPU server in tens of thousands of dollars.

In the first step, choose NVIDIA GPU cards to execute CUDA. One may refer to the specifications of the cards at the NVIDIA official website [12], and purchase the cards that fit the budget and that suit the computational needs. NVIDIA GeForce series is the most popular graphics card category in the public, readily available in computer stores. The most powerful GeForce single-GPU card to date is GTX 680, comprising a GPU chip with 1,536 CUDA cores. GTX 580 cards are used as a demonstration in this section instead.

Then, select a motherboard that supports 2 CPU chips and 4 pieces of 2-slot GPU cards, so that the server can undertake more computations concurrently while performing other tasks by CPU during GPU computation. Tyan S7025WAGM2NR motherboard is of such a type because it is mainly used in servers.

Given the selected Tyan motherboard, take 2 pieces of CPU for controlling the server system. Intel Xeon E5620 is the choice because it is the cheapest CPU for server-class computers to date, which has 4 cores each. So a server has altogether 8 CPU cores. A CPU core is required to control one GPU chip, so there are still 4 CPU cores remaining for other CPU-based tasks when all 4 GPU chips are performing computations. We bear in mind that CPU just helps to

bridge GPU with the operating system, so it is unnecessary to rely on it directly for GPU computations, so the choice of CPU is thus less important in a GPU server configuration in a tight budget.

Reserve enough random access memory (RAM) for the server. To the author's experience, a GPU should have 4 GB of random access memory for efficient data transfer between CPU and GPU, so that a server of 4 GPU cards should have at least a total of 16 GB memory for good computational performance. Note that error-correcting code (ECC) memory is needed for server-grade computers. In view of the memory requirement in GPU computation, an operating system of 64-bit version should be installed in order to utilize the 16 GB memory.

Assemble two hard drives for providing enough storage space. MD simulations involve generating phase space coordinates at each time step to find their time average, so it is worth spending more money on storage. The server uses 2 pieces of Hitachi 2 TB hard drives. A server thus contains 4 GB of storage; only a small portion goes to the operating system. After the operating system is installed on one hard drive, remember to mount the other drive to the operating system.

Adopt a power supply unit (PSU) capable of driving all GPU cards as well as other computer components. Check the power required for each component from their manuals beforehand to estimate the total power required at full load. To the author's experience, the PSU should be of the highest wattage one can find in an ordinary computer store. A 1500 W PSU, for example SilverStone

Strider 1500W, is one of the most powerful PSU's available in conventional computer stores to date. For safety, we must use only the power cords provided by the PSU in the assembly because they are more capable of withstanding the high current provided by the PSU.

Fig. 2.4 shows the bench test settings of the internal components. The components except the computer case are fully prepared and connected. The bench test is useful to inspect the functionality of the components in an easier way. Otherwise the components have to be fixed to or removed from the computer case during functionality checking.

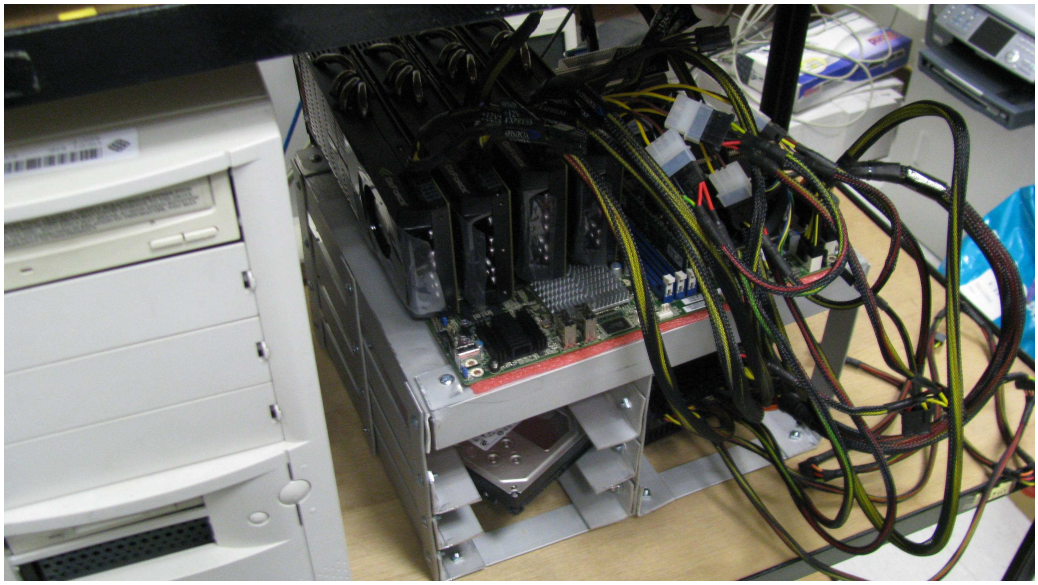

Fig. 2.4 – Bench testing of components before assembly on the computer case.

Beware of ventilation of GPU cards, especially when one wants to install multiple GPU cards in a single server. The easiest way to ensure good ventilation is use a computer case with more fans. Cooler Master HAF-X is such an example to date because it contains a big fan on the side cover that cools down the GPU cards. Fig. 2.5 shows the additional fans on the top and the side cover of the

computer case, which are the key features of enhanced cooling proposed by the Cooler Master HAF-X. In fact, an aluminum computer case is another choice in assembling a GPU server, as it can further remove heat by conduction. Fig. 2.6 shows the components assembled inside a computer case.

Fig. 2.5 – Two additional fans on the top and 1 additional fan on the side cover to ensure satisfactory cooling.

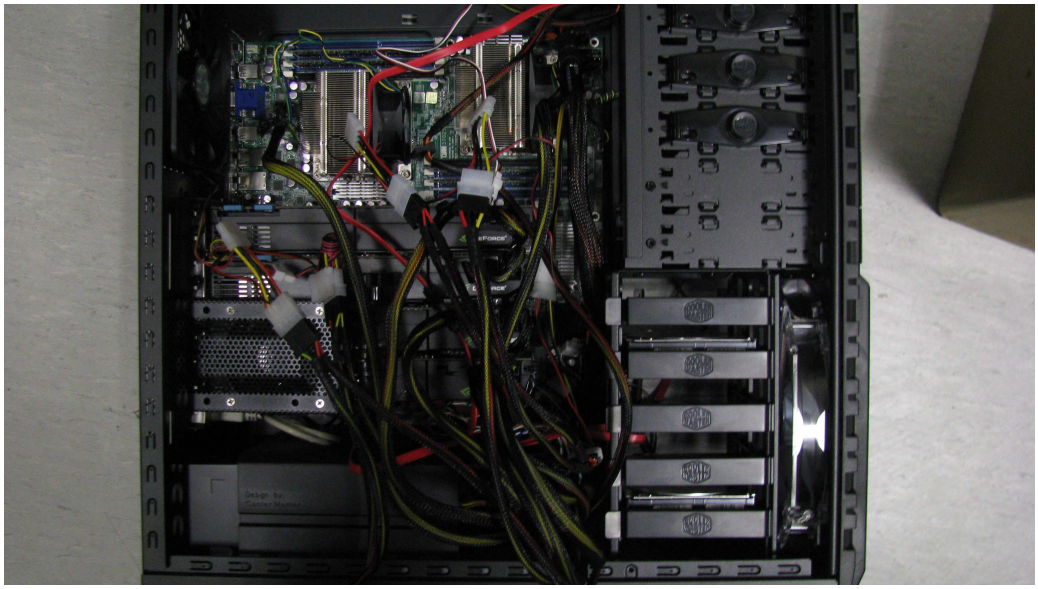

Fig. 2.6 – A GPU server with hardware components installed.

Install a free Linux operating system after assembly. To date, Ubuntu 12.04 LTS (64-bit version) is recommended because it can accommodate 4 GPU cards with minimum tuning, according to the author's experience. Another reason for using Ubuntu is its technical support from worldwide developers.

Download the required CUDA installers after the installation of Ubuntu 12.04 at CUDA Zone [13]. The whole set of installers should include the developer driver, CUDA toolkit, and CUDA GPU System Development Kit (SDK). The toolkit version to date is CUDA 4.2. One should install the developer driver first, followed by the toolkit and finally the SDK. Remember to confirm the completion of installation at the end by entering a command `nvcc -V` in the shell prompt. The version number of the CUDA toolkit installed would be displayed. A complete set of instructions detailing the installation steps can be found on the internet [14]. Fig. 2.7 is a set of 3 GPU servers, each with 4 double-slot GPU cards, connected by a KVM switch. Altogether there are 12 GPU cards, allowing 12 computation tasks concurrently with maximum performance.

One may check the temperature of each GPU card at runtime by typing `nvidia-smi -a` in the command prompt. The GPU cards should be below 50 °C in idle time, and around 90 °C in execution time. If the cards are too hot in execution time, one should consider storing the server in an air-conditioned room.

Fig. 2.7 – The complete set of GPU servers.

2.4 References

[1] F. Mandl, *Statistical Physics, 2nd ed.* (John Wiley & Sons, Essex, 1988).

[2] F. Reif, *Fundamentals of Statistical and Thermal Physics* (McGraw-Hill, New York, 1965).

[3] P.-W. Ma, C. H. Woo, and S. L. Dudarev, Phys. Rev. B **78**, 024434 (2008).

[4] P.-W. Ma, S. L. Dudarev, A. A. Semenov, and C. H. Woo, Phys. Rev. E **82**, 031111 (2010).

[5] S. Chiesa, P. M. Derlet, and S. L. Dudarev, Phys. Rev. B **79**, 214109 (2009).

[6] R. Kubo, Rep. Prog. Phys. **29**, 255 (1966).

[7] H. J. C. Berendsen, J. P. M. Postma, W. F. Van Gunsteren, A. Di Nola and J. R. Haak, J. Chem. Phys. **81**, 3684 (1984).

[8] M. P. Allen and D. J. Tildesley, *Computer Simulation of Liquids* (Oxford University Press, New York, 1987).

[9] P.-W. Ma and C. H. Woo, Phys. Rev. B **79**, 046703 (2009).

[10] D. B. Kirk and W. W. Hwu, *Programming Massively Parallel Processors – A Hands-on Approach* (Morgan Kaufmann, Burlington, 2010).

[11] NVIDIA, *NVIDIA CUDA C Programming Guide Version 4.0*, available on http://developer.download.nvidia.com/compute/cuda/4_0/toolkit/docs/CUDA_C_Programming_Guide.pdf

[12] NVIDIA, http://www.nvidia.com

[13] NVIDIA, http://developer.nvidia.com/category/zone/cuda-zone

[14] T. Arildsen and T. Larsen, *Installing CUDA Under Ubuntu 10.04*, available on http://wiki.accelereyes.com/wiki/index.php/Installing_CUDA_Under_Ubuntu_10.04

Chapter 3: Methodology

3.1 Simulation settings

In the following, the interatomic interaction in BCC iron is described by the magnetic many-body potential developed by Chiesa, Derlet and Dudarev (CDD) [1], based on the embedded atomic method (EAM) [2], in which the spins are all parallel at the ground state. In this regard, the interatomic potential U in the Hamiltonian of ferromagnetic iron,

$$H = \sum_i \frac{\boldsymbol{p}_i^2}{2m_i} + U\left(\{\boldsymbol{R}_i\}\right) - \frac{1}{2}\sum_{i,j} j_{ij}\left(\{\boldsymbol{R}_i\}\right)\boldsymbol{e}_i \cdot \boldsymbol{e}_j + g\mu_{\mathrm{B}} S\boldsymbol{H}^{\mathrm{ext}} \cdot \sum_i \boldsymbol{e}_i , \quad (3.1)$$

is implemented by

$$U\left(\{\boldsymbol{R}_i\}\right) = U_{\mathrm{CDD}}\left(\{\boldsymbol{R}_i\}\right) - \left(-\frac{1}{2}\sum_{i,j} j_{ij}\{\boldsymbol{R}_i\} \right), \quad (3.2)$$

to remove the ground state energy of the spin subsystem at absolute zero temperature, so that U is solely responsible for the lattice subsystem. The spin energy contribution to the Hamiltonian would then come from the spin vector $\boldsymbol{e}_i$. By doing so, the interatomic forces can be defined correctly at absolute zero temperature [3]. Therefore, the Hamiltonian becomes

$$\begin{aligned} H = & \sum_i \frac{\boldsymbol{p}_i^2}{2m_i} + U_{\mathrm{CDD}}\left(\{\boldsymbol{R}_i\}\right) + \frac{1}{2}\sum_{i,j} j_{ij}\left(\{\boldsymbol{R}_i\}\right)\left(1 - \boldsymbol{e}_i \cdot \boldsymbol{e}_j\right) \\ & + g\mu_{\mathrm{B}} S\boldsymbol{H}^{\mathrm{ext}} \cdot \sum_i \boldsymbol{e}_i \end{aligned} . \quad (3.3)$$

To investigate the temperature dependence of magnetic effect in spin-lattice coupled system, the cubic simulation cell containing 54000 iron atoms with spins was built up by a box of 30×30×30 BCC unit cells of about 85×85×85 $Å^3$, with periodic boundary conditions [4] applied to avoid the surface effects. The degrees of freedom of spin and lattice in the system were initialized at zero Kelvin by exposing the bulk to a fixed magnetic field along +*z* axis, whose magnitude ranges from 0 T to 1000 T. Later on, the system was thermalized at a given temperature, ranging from 300 K to 1400 K by Langevin thermostat [5] applied on both lattice and spins subsystems [3]. Suzuki-Trotter decomposition (STD) algorithm [6-11] was used for solving the equations of motion with the time-step being 1 femtosecond (fs), in order to obtain the phase space trajectory.

To determine the equilibrium atomic volume at a given temperature under non-stressed condition, the *NPT* ensemble was adopted with Berendsen barostat [12] and Langevin thermostat [5] respectively maintained at zero pressure and at a pre-set temperature. The thermalization time was set at least 2 ns, in order to allow the critical slowing down relaxation [13-14] of the spin subsystem to occur near the ferro/paramagnetic (FM/PM) phase boundary, with the time-step of 1 fs. After obtaining the equilibrium spin and lattice configurations, the atomic volume was calculated by ensemble average within the sampling time of 1 ns, from which the thermal expansion coefficient was determined.

In the calculations of magnetization and the related equilibrium thermodynamic quantities, i.e. energy etc., the *NVT* ensemble was adopted, where the atomic volume was chosen as the equilibrium one at the given temperature range mentioned above. The relaxation time and sampling time in

obtaining the statistical stationary data was similar as mentioned above to ensure the completion of the critical slowing down of spins.

3.2 Data Collection and Processing

1. Thermodynamic Properties

(i) Atomic Volume

Under the stress-free condition, the system is thermalized at a given temperature and applied external magnetic field, in which the equilibrium atomic volume is the result arising from the free energy minimized. In practice, the equilibrium atomic volume is derived from the relation $V^{\mathrm{eq}}\left(T,H^{\mathrm{ext}}\right)=\left\{a\left(T,H^{\mathrm{ext}}\right)\right\}^3/2$ for BCC crystal structure [15], where $a\left(T,H^{\mathrm{ext}}\right)$ is the equilibrium lattice parameter as the function of temperature T and external field H^{ext}. After equilibrium in the *NPT* ensembles, the lattice constant *a* of the bulks were obtained from the bulk dimensions for different temperatures and external magnetic field strengths by dividing the box length by the number of unit cells forming the BCC structure.

(ii) Magnetization and Energy

The atomic magnetization allows us to inspect spin collinearity, which relates to long range magnetic ordering. If the atomic magnetization approaches zero, long range magnetic ordering tends to vanish and the bulk turns to the paramagnetic state. Also, the spin-spin correlation functions and effective magnetic field strength per atom represent the short range magnetic ordering

around an atom, which would drop with decreasing spin correlation. On the other hand, the magnetic energy is a quantity specifying the response of spins to the external field, which changes the value of the spin-spin correlation function $\boldsymbol{e}_i \cdot \boldsymbol{e}_j$ and the atomic magnetization.

The atomic magnetization is determined by

$$M = \frac{1}{N}\left|\left\langle g\mu_{\mathrm{B}} S \sum_i e_i^z \right\rangle_{T^{\mathrm{eq}},V^{\mathrm{eq}}}\right|, \tag{3.4}$$

where the angle brackets $\langle\cdots\rangle_{T^{\mathrm{eq}},V^{\mathrm{eq}}}$ represent the ensemble average obtained at equilibrium temperature T^{eq} and equilibrium volume V^{eq}, N is the number of atoms in a system, S is the magnitude of a classical spin, and e_i^z is the z-component of the unit spin vector of atom i. On the other hand, the atomic magnetic energy from the Hamiltonian at T^{eq} and V^{eq} has the form of an ensemble average as

$$E^{\mathrm{magnetic}} = \frac{1}{N}\left\langle -\frac{1}{2}\sum_{i,j} j_{ij}\left(\{\boldsymbol{R}_i\}\right)\boldsymbol{e}_i \cdot \boldsymbol{e}_j + g\mu_{\mathrm{B}} S\boldsymbol{H}^{\mathrm{ext}} \cdot \sum_i \boldsymbol{e}_i \right\rangle_{T^{\mathrm{eq}},V^{\mathrm{eq}}}. \tag{3.5}$$

Again, bear in mind that the spin has an opposite direction to the magnetic moment.

In summary, the ensemble averages were obtained from the time averages, so that the magnetization and spin-spin correlation functions could be derived from the phase-space trajectories obtained from SLD simulations after the equilibrium spin and lattice configurations are achieved.

(iii) Vibrational Energy

The heat capacity can be derived from the vibrational energy at constant volume, which is associated with the heat absorbed during the corresponding thermodynamic process. The ensemble average of the vibrational energy is derived in two steps, according to its definition in Chapter 2. First we obtained the total energy $E\left(T^{\text{eq}},V^{\text{eq}}\right)$ at equilibrium from the *NPT* ensembles in terms of ensemble averaging. In the Hamiltonian used here, the total energy per atom can be written as

$$E\left(T^{\text{eq}},V^{\text{eq}}\right)=\frac{1}{N}\left\langle \begin{array}{l} \sum_i \frac{\boldsymbol{p}_i^2}{2m}+U_{\text{CDD}}\left(\{\boldsymbol{R}_i\}\right) \\ +\frac{1}{2}\sum_{i,j} j_{ij}\left(\{\boldsymbol{R}_i\}\right)\left(1-\boldsymbol{e}_i\cdot\boldsymbol{e}_j\right) \\ +g\mu_{\text{B}}S\boldsymbol{H}^{\text{ext}}\cdot\sum_i \boldsymbol{e}_i \end{array} \right\rangle_{T^{\text{eq}},V^{\text{eq}}} \tag{3.6}$$

The static energy E^{static} per atom is equal to the total energy of an atom at equilibrium volume $E\left(0,V^{\text{eq}}\right)$ and absolute zero temperature,

$$E^{\text{static}}=E\left(0,V^{\text{eq}}\right)=\frac{1}{N}\left[U_{\text{CDD}}\left(\left\{\boldsymbol{R}_i^0\right\}\right)-g\mu_{\text{B}}S\left|\boldsymbol{H}^{\text{ext}}\right|\right], \tag{3.7}$$

where $\left\{\boldsymbol{R}_i^0\right\}$ is the lattice configuration with all the lattice being frozen at their lattice sites at V^{eq}, and S is the magnitude of the spin vector. In this regard, the defined vibrational energy is associated with the energy increase due to the thermal fluctuations of the degrees of freedom of spin and lattice in the coupling system, expressed as

$$E^{\text{vib}} = E^{\text{tot}} - E^{\text{static}} = E\left(T^{\text{eq}}, V^{\text{eq}}\right) - E\left(0, V^{\text{eq}}\right). \quad (3.8)$$

2. Quantities Related to Derivative

The thermal expansion coefficient comes from the temperature derivative of volume, whereas the heat capacity from that of vibrational energy, both of which are solved numerically from simulation results. However, numerical differentiation is sensitive to fluctuation of data points, which could lead to a large variation of the trend of the derivatives. Data smoothing is thus necessary to interpolate more data points and to provide a more gentle transition between successive data points; a smoother yet reliable trend of the derivative would be obtained afterwards.

(i) Heat Capacity

Temperature dependence of the heat capacity can characterize the second-order phase transition by identifying the temperature of abrupt change or of divergence.

The heat capacity at constant pressure P, known as C_P, was found by [16]

$$C_P = \left(\frac{\mathrm{d}Q}{\mathrm{d}T}\right)_P = \left(\frac{\partial E^{\text{vib}}}{\partial T}\right)_P, \quad (3.9)$$

where Q is the heat absorbed, and T is the absolute temperature, obtained from the derivative of the vibrational energy with respect to temperature. In determining the heat absorbed at equilibrium volume, the vibrational energy E^{vib}

is used instead. There are as many such curves as the number of magnetic field strength attempted.

(ii) Thermal Expansion Coefficient

Just as the atomic volume can realize the magnetic effect of materials on temperature and field strength, the thermal expansion coefficient is another such quantity. This coefficient is a derivative which enables us to visualize the volume change more clearly than using the atomic volume, and the peaks on the derivative curve also indicate the transition temperature at which the magnetic ordering is no longer varied by temperature.

The thermal expansion coefficient α at constant pressure P was evaluated as [17], i.e.

$$\alpha = \frac{1}{V}\left(\frac{\mathrm{d}V}{\mathrm{d}T}\right)_P, \tag{3.10}$$

where V is the instantaneous volume at temperature T and $P = 0$ throughout the simulations in the thesis. The coefficient was found by first finding the atomic volume against temperature, and then by evaluating the derivative of the atomic volume with respect to temperature. After that, the derivative obtained was divided by the atomic volume at its corresponding temperature. There are also as many such curves as the number of magnetic fields attempted.

3. Thermal Excitations Spectra

(i) Magnon Density of States

When a classical spin rotates about its axis of rotation at a finite temperature, it generates a spin wave, whose quantization is called a magnon. Fig. 3.1 shows the generation of a spin wave of one wavelength long by collective spin precession.

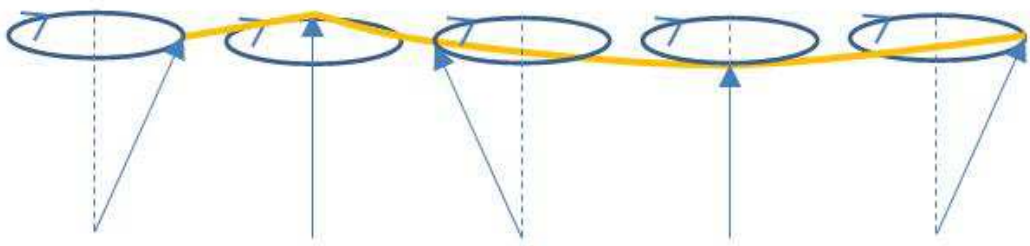

Fig. 3.1 – Spin wave formation. The orange line represents a spin wave generated by collective spin precession.

The solution to the spin equation of motion in one dimension can be obtained as below. The energy of a classical spin $\boldsymbol{S}_n$ with index n is

$$E_n = -2J\boldsymbol{S}_n \cdot \left(\boldsymbol{S}_{n-1} + \boldsymbol{S}_{n+1}\right), \tag{3.11}$$

where J is the exchange integral. Since the magnetic moment is $\boldsymbol{\mu}_n = -g\mu_{\mathrm{B}}\boldsymbol{S}_n$, the above equation is rewritten as

$$E_n = -\boldsymbol{\mu}_n \cdot \left[\frac{-2J}{g\mu_{\mathrm{B}}}\left(\boldsymbol{S}_{n-1} + \boldsymbol{S}_{n+1}\right)\right]. \tag{3.12}$$

By comparing with $E_n = -\boldsymbol{\mu}_n \cdot \boldsymbol{H}_n^{\text{eff}}$, where $\boldsymbol{H}_n^{\text{eff}}$ is the effective magnetic field on $\boldsymbol{S}_n$, one may get

$$\boldsymbol{H}_n^{\text{eff}} = \frac{-2J}{g\mu_{\text{B}}}\left(\boldsymbol{S}_{n-1} + \boldsymbol{S}_{n+1}\right). \tag{3.13}$$

The equation of motion of classical spins is

$$\begin{aligned}\dot{\boldsymbol{S}}_n &= \frac{1}{\hbar}\boldsymbol{\mu}_n \times \boldsymbol{H}_n^{\text{eff}} \\ &= -\frac{1}{\hbar} g\mu_{\text{B}} \boldsymbol{S}_n \times \frac{-2J}{g\mu_{\text{B}}}\left(\boldsymbol{S}_{n-1} + \boldsymbol{S}_{n+1}\right) \\ &= \frac{2J}{\hbar}\boldsymbol{S}_n \times \left(\boldsymbol{S}_{n-1} + \boldsymbol{S}_{n+1}\right).\end{aligned} \tag{3.14}$$

Approximation is necessary for solving it. First we resolve $\dot{\boldsymbol{S}}_n$ into Cartesian components as

$$\dot{S}_n^x = \frac{2J}{\hbar}\left[S_n^y\left(S_{n-1}^z + S_{n+1}^z\right) - S_n^z\left(S_{n-1}^y + \mathrm{S}_{n+1}^y\right)\right], \tag{3.15}$$

$$\dot{S}_n^y = -\frac{2J}{\hbar}\left[S_n^x\left(S_{n-1}^z + S_{n+1}^z\right) - S_n^z\left(S_{n-1}^x + S_{n+1}^x\right)\right], \tag{3.16}$$

$$\dot{S}_n^z = \frac{2J}{\hbar}\left[S_n^x\left(S_{n-1}^y + S_{n+1}^y\right) - S_n^y\left(S_{n-1}^x + S_{n+1}^x\right)\right]. \tag{3.17}$$

Here, S_n^α is the Cartesian component of $\boldsymbol{S}_n$ ($\alpha = x, y, z$). Then we assume that only small excitation exists, i.e. $S_n^x, S_n^y \ll S$. Then we have $S_n^z = S$, and ignore the cross terms due to S_n^x and S_n^y. So,

$$\dot{S}_n^x = \frac{2J}{\hbar}\left[2S_n^y - S_{n-1}^y - S_{n+1}^y\right], \tag{3.18}$$

$$\dot{S}_n^y = -\frac{2J}{\hbar}\left[2S_n^x - S_{n-1}^x - S_{n+1}^x\right], \tag{3.19}$$

$$\dot{S}_n^z = 0\,. \tag{3.20}$$

We expect a wavelike solution to it again as

$$S_n^x = A\exp\left[i\left(nqa-\omega t\right)\right];\quad S_n^y = B\exp\left[i\left(nqa-\omega t\right)\right],\quad . \tag{3.21}$$

where q is the wave-vector, A and B are constants, ω is the spin wave frequency, t is time, i is the imaginary unit, and a is the lattice constant. By substituting the wavelike solutions in Eq. (3.21) into Eqs. (3.18) and (3.19), two expressions are obtained:

$$\begin{aligned} -i\omega A &= \frac{2JS}{\hbar}\left[2-\exp\left(-iqa\right)-\exp\left(iqa\right)\right]B \\ &= \frac{4JS}{\hbar}\left(1-\cos qa\right)B; \end{aligned} \tag{3.22}$$

$$\begin{aligned} -i\omega B &= -\frac{2JS}{\hbar}\left[2-\exp\left(-iqa\right)-\exp\left(iqa\right)\right]A \\ &= -\frac{4JS}{\hbar}\left(1-\cos qa\right)A. \end{aligned} \tag{3.23}$$

We again require non-trivial solutions to A and B, so

$$\begin{vmatrix} i\omega & \frac{4JS}{\hbar}\left(1-\cos qa\right) \\ -\frac{4JS}{\hbar}\left(1-\cos qa\right) & i\omega \end{vmatrix} = 0\,, \tag{3.24}$$

or

$$\hbar\omega = 4JS\left(1-\cos qa\right). \tag{3.25}$$

Eq. (3.25) returns the dispersion relation of spin waves. When only long wavelengths exist, $qa \ll 1$. The dispersion relation reduces to

$$\hbar\omega = \left(2JSa^2\right)q^2, \tag{3.26}$$

which can be expressed as

$$\omega = Dq^2;\ D = \frac{2JSa^2}{\hbar}. \tag{3.27}$$

Here, D is called the spin wave stiffness, characterizing the tendency of the classical spin to deviate from perfect alignment. A high value of D shows that the spin tends to stay aligned with its easy direction. In fact, the above derivations apply to a cubic lattice by considering nearest-neighbor interactions [18], forming the basis of the discussions of body-centered cubic (BCC) lattices in later chapters.

To indicate the amplitude of the spin waves at different frequencies, the power spectrum of magnons, known as the magnon spectrum, can be obtained from the time-dependent autocorrelation function of the spin moment. In practice, the normalized autocorrelation function is

$$R_{\text{spin}}(t) = \frac{\langle \boldsymbol{e}_i(t) \cdot \boldsymbol{e}_i(0) \rangle}{\langle \boldsymbol{e}_i(0) \cdot \boldsymbol{e}_i(0) \rangle} = \frac{\langle \boldsymbol{e}_i(t) \cdot \boldsymbol{e}_i(0) \rangle}{|\boldsymbol{e}_i(0)|^2}. \tag{3.28}$$

This is similar to understanding the lattice wave, whose quantization is called a phonon, using a phonon spectrum generated from the normalized velocity autocorrelation function (VACF) expressed as

$$R_{\text{velocity}}(t) = \frac{\langle \boldsymbol{v}_i(t) \cdot \boldsymbol{v}_i(0) \rangle}{\langle \boldsymbol{v}_i(0) \cdot \boldsymbol{v}_i(0) \rangle} = \frac{\langle \boldsymbol{v}_i(t) \cdot \boldsymbol{v}_i(0) \rangle}{|\boldsymbol{v}_i(0)|^2}, \tag{3.29}$$

where $\boldsymbol{v}_i$ is the atomic velocity of atom i.

The power spectrum generated by this way is also called the density of states (DOS), which represents the relative strengths of phonon and magnon frequencies, or energy levels, available in the time-varying phonon and magnon waves, respectively.

Readers may refer to signal processing texts such as that by Proakis and Manolakis [19] for a detailed mathematical exposition of power spectra. Here, just a brief idea of the method in calculating the phonon and magnon spectra is presented. The autocorrelation function of a time-dependent stochastic signal $x(t)$ representing some vibrational quantity, such as atomic velocity and spin wave amplitude, is defined as

$$R(\tau)=\int_{-\infty}^{+\infty} x(t)\,x(t+\tau)\,\mathrm{d}t\,, \tag{3.30}$$

which gives the information about the similarity between the values of x at time t and at time τ later. According to Wiener-Khintchine theorem [20], the Fourier transform of $R(\tau)$ returns the power spectral density or the power spectrum $G(\omega)$ of $x(t)$ as

$$G(\omega)=\int_{-\infty}^{+\infty} R(\tau)e^{i\omega t}\mathrm{d}t\ , \tag{3.31}$$

where i is the imaginary unit, showing the signal power at a certain frequency.

In the thesis, the autocorrelation of spin moment may not fluctuate around zero at finite temperature in the ferromagnetic phase, at which the spin waves exhibit stronger long range ordering, and hence a larger spin correlation. However, we are concerned about the time-varying component of spin waves in the physical point of view. In this regard, the magnon spectrum should have the direct current (DC) component removed, which represents the shift of the waveform value in time domain to zero on average, achieved by subtracting the average value of the autocorrelation under the amplitude-time curve from the instantaneous amplitude.

After the shifted amplitude-time curve was obtained, the DOS was generated using the Fast Fourier transform (FFT) algorithm in 2^{14} = 16384 points, which should be enough to analyze the spectral behavior of spin waves. According to the simulation results, an FFT in over 16384 points has no further improvement

in the resulting spectra; a higher frequency resolution is unnecessary in the current work.

(ii) Magnon Dispersion Relations

A magnon dispersion relation shows the magnon energy against wave-vector, which is measured on the reciprocal lattice established by the Fourier transform of the direct lattice in the spatial domain. Expressed in the reciprocal domain, a quantity $n(\boldsymbol{r})$ in the direct lattice with translation symmetry, determined by position $\boldsymbol{r}$, has the form

$$n(\boldsymbol{r}) = \sum_{\boldsymbol{G}} n_{\boldsymbol{G}} \exp(i\boldsymbol{G}\cdot\boldsymbol{r}), \tag{3.32}$$

where $\boldsymbol{G}$ is a reciprocal lattice vector for a given structure, and $n_{\boldsymbol{G}}$ is the complex coefficient of Fourier series for each $\boldsymbol{G}$ in the reciprocal lattice. The wave-vectors to be mentioned in the derivation of the magnon dispersion relations are simply the $\boldsymbol{G}$'s in the reciprocal domain.

In addition, the reciprocal lattice is usually represented by the first Brillouin zone, defined as the Wigner-Seitz cell of a reciprocal lattice point, bounded by the perpendicular planes in the midway between that point and each neighboring reciprocal lattice point. It is known that the standard primitive vectors in the direct BCC lattice, expressed in Cartesian coordinates using the lattice constant a, are

$$\boldsymbol{a}_1 = \left(-\frac{1}{2}a, \frac{1}{2}a, \frac{1}{2}a\right),\ \boldsymbol{a}_2 = \left(\frac{1}{2}a, -\frac{1}{2}a, \frac{1}{2}a\right),\ \boldsymbol{a}_3 = \left(\frac{1}{2}a, \frac{1}{2}a, -\frac{1}{2}a\right), \tag{3.33}$$

expressed in Fig. 3.2.

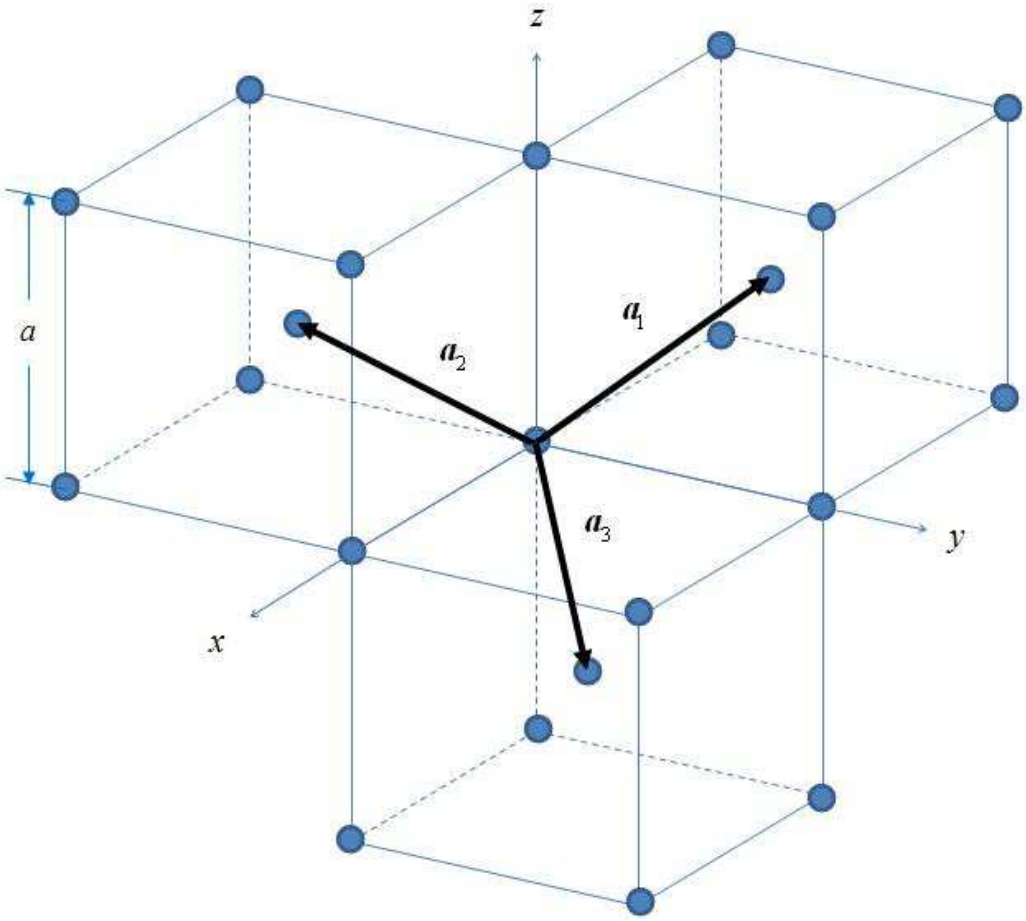

Fig. 3.2 – Primitive lattice vectors of a BCC structure.

Then, the primitive vectors in the reciprocal BCC structure, defined by

$$\boldsymbol{b}_1 = 2\pi \frac{a_2 \times a_3}{a_1 \cdot a_2 \times a_3}\,,\ \boldsymbol{b}_2 = 2\pi \frac{a_3 \times a_1}{a_1 \cdot a_2 \times a_3}\,,\ \boldsymbol{b}_3 = 2\pi \frac{a_1 \times a_2}{a_1 \cdot a_2 \times a_3}\,, \tag{3.34}$$

become

$$\boldsymbol{b}_1 = 2\pi\left(0, \frac{1}{a}, \frac{1}{a}\right),\ \boldsymbol{b}_2 = 2\pi\left(\frac{1}{a}, 0, \frac{1}{a}\right),\ \boldsymbol{b}_3 = 2\pi\left(\frac{1}{a}, \frac{1}{a}, 0\right). \tag{3.35}$$

For a BCC structure, there are four major points on the first Brillouin zone: Γ being the origin, H being the edge on [100] direction, P being the edge on [111] direction, and N being a point in [110] direction. The direction Δ represents that from Γ to H, Λ from Γ to P, and Σ from Γ to N. Other high symmetry points and directions of a BCC reciprocal lattice are given in Table 3.1.

Label	Cartesian Coordinates	Lattice Coordinates	Range of x
Γ	$\frac{2\pi}{a}(0,0,0)$	0	N/A
H	$\frac{2\pi}{a}(0,1,0)$	$\frac{1}{2}(\boldsymbol{b}_1-\boldsymbol{b}_2+\boldsymbol{b}_3)$	N/A
P	$\frac{\pi}{a}(1,1,1)$	$\frac{1}{4}(\boldsymbol{b}_1+\boldsymbol{b}_2+\boldsymbol{b}_3)$	N/A
N	$\frac{\pi}{a}(1,1,0)$	$\frac{1}{2}\boldsymbol{b}_3$	N/A
Δ	$\frac{2\pi}{a}(0,x,0)$	$\frac{1}{2}x(\boldsymbol{b}_1-\boldsymbol{b}_2+\boldsymbol{b}_3)$	$0<x<1$
F	$\frac{\pi}{a}(x,(2-x),x)$	$\frac{1}{4}((2-x)\boldsymbol{b}_1+(3x-2)\boldsymbol{b}_2+(2-x)\boldsymbol{b}_3)$	$0<x<1$
Λ	$\frac{\pi}{a}(x,x,x)$	$\frac{1}{4}x(\boldsymbol{b}_1+\boldsymbol{b}_2+\boldsymbol{b}_3)$	$0<x<1$
Σ	$\frac{\pi}{a}(x,x,0)$	$\frac{1}{2}x\boldsymbol{b}_3$	$0<x<1$
D	$\frac{\pi}{a}(1,1,x)$	$\frac{1}{4}(x\boldsymbol{b}_1+x\boldsymbol{b}_2+(2-x)\boldsymbol{b}_3)$	$0<x<1$

Table 3.1 – High symmetry points in a BCC reciprocal lattice.

Fig. 3.3 shows the first Brillouin zone containing points and directions in Table 3.1.

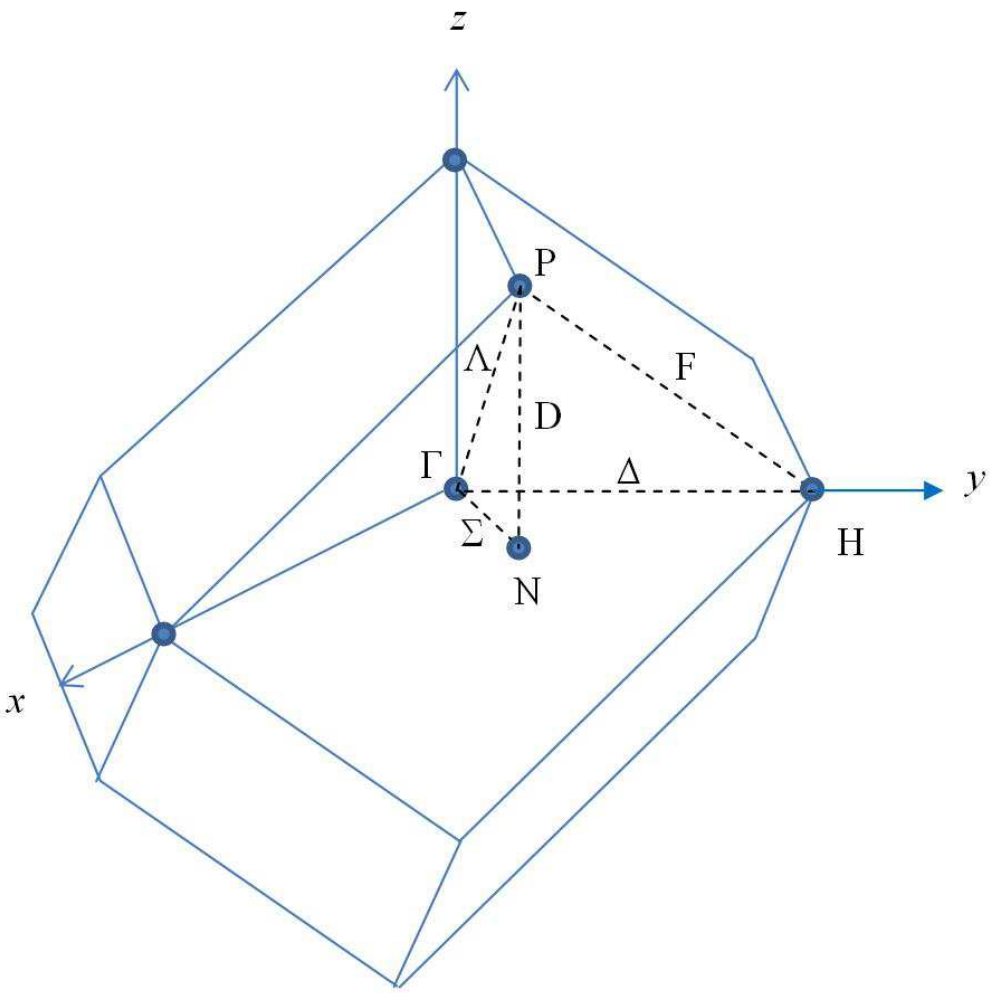

Fig. 3.3 – First Brillouin zone of a BCC structure.

The reciprocal lattice is helpful to obtain the spin stiffness for various field strengths, which are represented by the magnon dispersion relation. For a description of the method of obtaining dispersion relations, one may refer to the text by Kittel [21] and Dove [22] for the theory behind it. Below is a brief discussion of the concept.

For an atom m, the spin wave S_m^x along the x-component can be expressed in a reciprocal lattice by

$$S_m^x(t) = \sum_{\boldsymbol{q}} S_m^x(\boldsymbol{q}) \exp\left[i\left(\boldsymbol{q}\cdot\boldsymbol{r}_m - \omega_{\boldsymbol{q}} t\right)\right], \tag{3.36}$$

where $S_m^x(\boldsymbol{q})$ is the amplitude of the spin wave of atom m with frequency $\omega_{\boldsymbol{q}}$ and wave-vector $\boldsymbol{q}$ along the x-component, $\boldsymbol{r}_m$ is the position vector of atom m, and t is time. Inverse Fourier transform of the reciprocal domain is applied to Eq. (3.36) to obtain

$$S_m^x(\boldsymbol{q}) = \frac{1}{N}\sum_{m=1}^{N} S_m^x(t) \exp\left(-i\boldsymbol{q}\cdot\boldsymbol{r}_m - \omega_{\boldsymbol{q}} t\right), \tag{3.37}$$

where N is the total number of atoms in a system.

By the definitions of the reciprocal lattice vectors, the smallest interval of a wave-vector for each Cartesian direction is

$$\Delta q_x = \frac{2\pi}{Na}(1,0,0),\ \Delta q_y = \frac{2\pi}{Na}(0,1,0),\ \Delta q_z = \frac{2\pi}{Na}(0,0,1). \tag{3.38}$$

Then the wave-vectors along the three major directions, Δ, Λ, and Σ are

$$\Delta : \Delta q_l = \frac{2\pi}{Na}(0,k,0) \text{ for } l = 0,1,2,\cdots,N; \tag{3.39}$$

$$\Lambda : \Delta q_l = \frac{2\pi}{Na}(k,k,k) \text{ for } l = 0,1,2,\cdots,\frac{N}{2}; \tag{3.40}$$

$$\Sigma : \Delta q_l = \frac{2\pi}{Na}(k,k,0) \text{ for } l = 0,1,2,\cdots,\frac{N}{2}. \tag{3.41}$$

Since a BCC lattice has an isotropic structure, it is just necessary to inspect the magnon dispersion relation on, for example, the [100] direction on a Brillouin zone (Δ in Fig. 3.3) which can basically describe the whole structure.

In practice, the dispersion relation graph could be generated from a given DOS by locating the frequency (i.e. energy) at which the peaks exist. We then transformed the peak indices as the wave-vectors, given by

$$\boldsymbol{q} = \frac{2\pi}{a}\left(\frac{l_1}{N_1}, \frac{l_2}{N_2}, \frac{l_3}{N_3}\right), \tag{3.42}$$

where N_1, N_2, and N_3 are unit cell dimensions in *x*-, *y*-, and *z*-directions, respectively, and l_1, l_2, and l_3 are positive integers smaller than N_1, N_2, and N_3. For example, in a cubic box of 30 unit cells along each dimension, the first six peaks in the magnon spectrum have the wave-vectors

$$\boldsymbol{q}_1 = \frac{2\pi}{30a}(1,0,0),\ \boldsymbol{q}_2 = \frac{2\pi}{30a}(1,1,0),\ \boldsymbol{q}_3 = \frac{2\pi}{30a}(1,1,1),$$

$$\boldsymbol{q}_4 = \frac{2\pi}{30a}(2,0,0),\ \boldsymbol{q}_5 = \frac{2\pi}{30a}(2,1,0),\ \boldsymbol{q}_6 = \frac{2\pi}{30a}(2,1,1). \tag{3.43}$$

The magnitude of the wave-vectors can be found by all these values of $\boldsymbol{q}$'s. After that, the magnon energy against the norm of the wave-vectors were plotted to obtain the dispersion relations.

3.3 References

[1] S. Chiesa, P. M. Derlet, and S. L. Dudarev, Phys. Rev. B **79**, 214109 (2009).

[2] M. S. Daw and M. I. Baskes, Phys. Rev. B **29**, 6443 (1984).

[3] P.-W. Ma, C.H. Woo, and S.L. Dudarev, Phys. Rev. B **78**, 024434 (2008).

[4] M. P. Allen and D. J. Tildesley, *Computer Simulation of Liquids* (Oxford University Press, 1987).

[5] W. F. Brown Jr., Phys. Rev. **130**, 1677 (1963).

[6] I. P. Omelyan, I. M. Mryglod, and R. Folk, Phys. Rev. Lett. **86**, 898 (2001).

[7] I. P. Omelyan, I. M. Mryglod, and R. Folk, Phys. Rev. E **64**, 016105 (2001).

[8] I. P. Omelyan, I. M. Mryglod, and R. Folk, Phys. Rev. E **66**, 026701 (2002).

[9] S. H. Tsai, M. Krech, and D. P. Landau, Brazil. J. Phys. **34**, 382 (2004).

[10] S. H. Tsai, H. K. Lee, and D. P. Landau, Am. J. Phys. **73**, 615 (2005).

[11] N. Hatano and M. Suzuki, Lect. Notes Phys. **679**, 37 (2005).

[12] H. J. C. Berendsen, J. P. M. Postma, W. F. Van Gunsteren, A. Di Nola and J. R. Haak, J. Chem. Phys. **81**, 3684 (1984).

[13] M. Dudka, R. Folk, Yu. Holovatch, and G. Moser, Condens. Matter Phys. **8**, 737 (2005).

[14] M. J. Dunlavy and D. Venus, Phys. Rev. B **69**, 094411 (2004).

[15] J. de Launay, J. Chem. Phys. **22**, 1676 (1954).

[16] G. Liebfried and W. Ludwig, Solid State Phys. **12**, 275 (1961).

[17] C. Wei, D. Srivastava, and K. Cho, Nano Lett**. 2**, 647 (2002).

[18] C. Kittel, *Introduction to Solid State Physics, 8th ed.* (Wiley, New York, 2005), p. 333.

[19] J. G. Proakis and D. K. Manolakis, *Digital Signal Processing, 3rd ed.* (Prentice Hall, New Jersey, 1996), p. 230.

[20] R. K. Pathria, *Statistical Mechanics, 2nd ed.* (Butterworth-Heinemann, Oxford, 1996), p. 474.

[21] C. Kittel, *Introduction to Solid State Physics, 8th ed.* (Wiley, New York, 2005).

[22] M. T. Dove, *Introduction to Lattice Dynamics* (Cambridge University Press, 1993).

Chapter 4: Results and Discussions

4.1 Introduction

This chapter considers the effect of an external magnetic field on the magnetic properties in the coupled spin and lattice system, i.e. BCC iron, by performing large-scale spin-lattice dynamics (SLD) simulations. The discussion starts from the external field effect on the long range magnetic ordering and the transition temperature, which exhibit a direct response to an external field. Then, the resulting transition temperatures should help to investigate the reduced temperature dependence of magnetization, and to show its relation with the applied field strength. The analysis of long range ordering helps to demonstrate the drawback of the mean field theory (MFT) to model ground state magnetic energy and reduced magnetization. Similarly, the short range magnetic ordering is another direct response to an external field, which can be represented by the spin-spin correlation functions and the effective magnetic field strength. Next, the discussion goes to the external field effect of magnons, in an attempt to analyze the magnetic ordering by considering magnon-magnon interaction and by interpreting the magnon density of states and the magnon dispersion relations. In addition, temperature dependence of the spin stiffness and of the uniform precession mode, both derived from the magnon dispersion relations, help to illustrate the field-induced magnetic ordering. Changes in magnetic ordering would result in the magneto-volume effect caused by the spin-lattice coupling, which is discussed in the last section of this chapter. Temperature dependence of the heat capacity and thermal expansion coefficient, obtained from the magneto-

volume effect, are used to demonstrate the external field effect. An explanation of the field-induced magneto-volume effect is presented finally by integrating the observations in this chapter.

4.2 Effects on Classical Spins

1. Long Range Magnetic Ordering

The long range magnetic ordering refers to the presence of correlation in the atomic spin alignment at large distances. The ordering is high if the spins separated by a large distance are still aligned in a similar direction. However, if the ordering is low for a large separation, the system is disordered. In a bulk of ferromagnetic iron, the long range magnetic ordering is represented by the macroscopic magnetization. It is common to express the overall magnetization using the mean field theory (MFT), which is a method to treat the interaction between atomic spins, called the exchange field, as coming from an external magnetic field. The idea of MFT is to simplify the many-body interactions, with each atom experiencing an effective field, to a one-body problem characterized by just a mean field. Since there is only one mean field, MFT has ignored the spin correlation along the directions other than the spin precession direction, making this approximation less accurate. Fortunately, SLD has already been developed as a tool to improve the shortcoming of MFT because SLD essentially considers spin motions including those along precession directions.

In the following, we first provide a brief introduction of MFT. Then we then present the results of SLD and compare it with the predictions of MFT, in an

attempt to analyze the cooperative effect of spins. The temperature dependence of magnetization will be adopted as a measure of both SLD and MFT for a comparison with the resulting Curie temperatures.

MFT assumes that each atom is exerted by an exchange field $\boldsymbol{B}_{\mathrm{E}}$ related to the magnetization $\boldsymbol{M}$ proportionally as

$$\boldsymbol{B}_{\mathrm{E}} = \lambda \boldsymbol{M} , \tag{4.1}$$

where λ is a temperature-independent mean field constant. The magnetic susceptibility χ can then be related to λ and current temperature T by

$$\chi = \frac{M}{H^{\mathrm{ext}}} = \frac{C}{T - T_{\mathrm{C}}} , \tag{4.2}$$

where $T_{\mathrm{C}} = C\lambda$ is the Curie temperature. Here, H^{ext} is the external magnetic field strength, and C is the Curie constant depending on the material.

According to MFT, the connection between the exchange integral J and the Curie temperature in quantum mechanics is given by

$$J = \frac{3k_{\mathrm{B}}T_{\mathrm{C}}}{2zS\left(S+1\right)} , \tag{4.3}$$

where z is the number of nearest neighbor atoms, k_{B} is the Boltzmann constant, and S is the spin quantum number. It can be understood from Eq. (4.3) that the magnetic energy experienced by each atom can be related to the Curie temperature by

$$zJS\left(S+1\right)=\frac{3}{2}k_{\mathrm{B}}T_{\mathrm{C}}. \tag{4.4}$$

The left hand side of Eq. (4.4) represents the atomic magnetic energy because it is the sum of the magnetic energy $E_{0\mathrm{K}}^{\mathrm{mag}}=zJS\left(S+1\right)$ for all z neighbor atoms. The proportionality constant between the atomic magnetic energy and T_{C}, according to MFT, is thus $3k_{\mathrm{B}}/2$.

In addition, under MFT, the temperature dependence of magnetization in ferromagnetic materials can be derived from the molecular field [1-3]. Suppose that an atom experiences the effective magnetic field strength $\boldsymbol{H}^{\mathrm{eff}}$ along the z-component, whose magnitude is H_z^{ext}. Then the normalized mean field magnetization $e^z\equiv M\left(T\right)/M\left(0\right)$ is obtained by iteration starting from an initial guess of 1, using

$$e^z=\frac{\exp\left(\zeta\right)+\exp\left(-\zeta\right)}{\exp\left(\zeta\right)-\exp\left(-\zeta\right)}-\frac{1}{\zeta}, \tag{4.5}$$

where $\zeta=g\mu_{\mathrm{B}}H^{\mathrm{eff}}/k_{\mathrm{B}}T$ with $H^{\mathrm{eff}}=\frac{1}{g\mu_{\mathrm{B}}}e^z\sum_i J_{ij}-H_z^{\mathrm{ext}}$, until convergence is attained. For BCC iron, the exchange integral in the effective field experienced by atom j, $\sum_i J_{ij}\left(R_{ij}\right)$, dependent on lattice separation R_{ij}, is determined by

$$\sum_i J_{ij}\left(R_{ij}\right)=8J_{ij}\left(\sqrt{3}a/2\right)+6J_{ij}\left(a\right), \tag{4.6}$$

where $8J_{ij}\left(\sqrt{3}a/2\right)$ represents the integral due to first nearest neighbor (1nn) atoms and $6J_{ij}\left(a\right)$ the integral due to second nearest neighbor (2nn) atoms.

Similar to MFT, SLD is another method to evaluate the temperature dependence of average magnetization by simulations in atomic level. Based on the Curie temperature expression for MFT in Eq. (4.4), it is possible that the magnetic energy at absolute zero temperature, called the ground state magnetic energy $E_{0\mathrm{K}}^{\mathrm{mag}}$, from SLD calculation should also be able to form at least an empirical relation to the transition temperature.

This section will compare the SLD simulation results with the MFT counterpart by observing the temperature dependence of field-induced magnetization to obtain the corresponding transition temperature. Then the section compares the atomic magnetic energy and the reduced magnetization found by both methods. After the analysis, it is believed that the ability of SLD to model ferromagnetic iron more closely to experimental results comes from its consideration of spin precession in forming the collective spin wave, which is not so in MFT.

(i) Magnetization

Magnetization, related to long range magnetic ordering, is about the collinearity of the spins microscopically. As is known, the magnetization in zero-field ferromagnetic iron is temperature-dependent, which vanishes at ferro/paramagnetic (FM/PM) phase boundary. In addition, the external field also affects the magnetization. Fig. 4.1 shows the temperature dependence of atomic

magnetization M in μ_B under various external fields ranging from 0 T to 1000 T. The overall magnetization for all field strengths drops with increasing temperature, starting with $2.2\mu_B$ at 0 Kelvin, but a stronger field results a higher magnetization, whose effect is found to be more apparent at higher temperature range attempted. One may observe the inflexion point of the magnetization curve by inspection, at which the curve changes its convexity, to represent the phase transition temperatures [4-5] and to understand its change due to the external field. The inflexion points observed from Fig. 4.1 are about 1020 K at 0 T, 1025 K at 10 T, 1050 K at 50 T, 1090 K for 100 T, and far beyond 1400 K at 1000 T. In fact, the inflexion point of the zero-field magnetization occurs at the temperature where long range magnetic ordering vanishes, hence the conventional definition of the Curie temperature of the zero-field condition. Since the inflexion point from the zero-field magnetization is close to the Curie temperature of body-centered cubic (BCC) Fe at 1043 K, it is believed that the points of inflexion for other field-induced magnetization curves should also relate to their respective FM/PM phase transition, which will be discussed later.

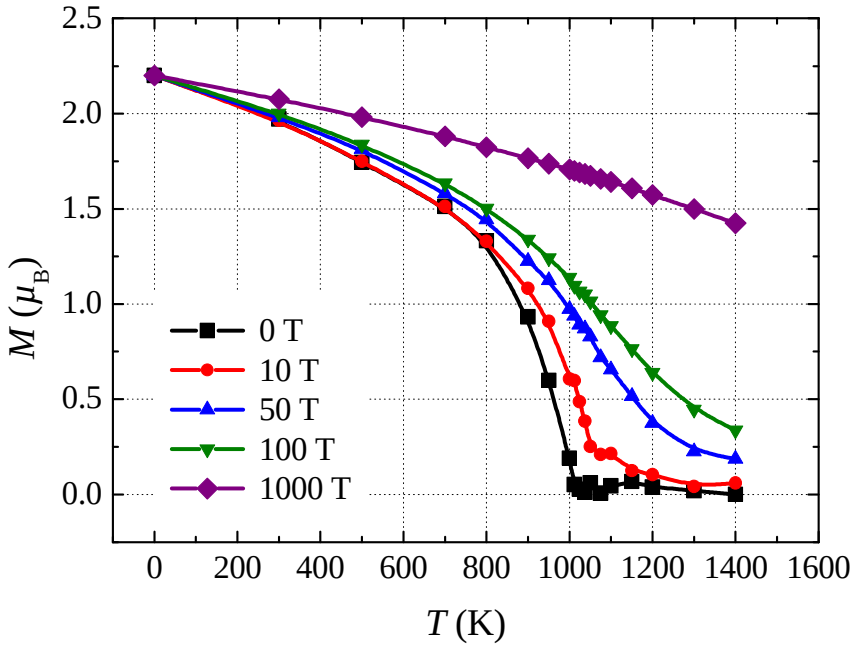

Fig. 4.1 – Atomic magnetization along the z-component for various magnetic fields tried. The transition temperatures, determined as the points of inflexion, increases with the field.

Instead of using Fig. 4.1, the overall effect of the external field can be visualized more clearly in Fig. 4.2, which shows the reduced magnetization $M(T)/M(0)$ against the reduced temperature T/T_C for various external fields attempted (0 T, 10 T, 50 T, and 100 T), where T_C's are the corresponding inflexion points. Experimental data under zero-field condition by Crangle and Goodman [6] are also presented as a comparison. It is noted that the SLD simulation results are departed from the experimental result because the quantum spins are treated classically in the SLD formulation [7]. First, one can notice that the reduced magnetization has nearly the same temperature dependence below $\sim 0.9T_C$, meaning that the external field has little effect on the reduced magnetization below the transition temperatures determined this way. On the

other hand, the effect of the external field on reduced magnetization starts to become more prominent near the beginning of the critical region at around $0.9T_C$, at which the magnetization is maintained above zero in the presence of an external field. Besides, a stronger external field would retard the abrupt drop of magnetization in the critical region more effectively. Comparing to the trend of the zero-field reduced magnetization, because the field-induced reduced magnetization starts to drop more abruptly around the T_C's determined above, the role of the inflexion points on the field-induced magnetization curves to represent the transition points is supported.

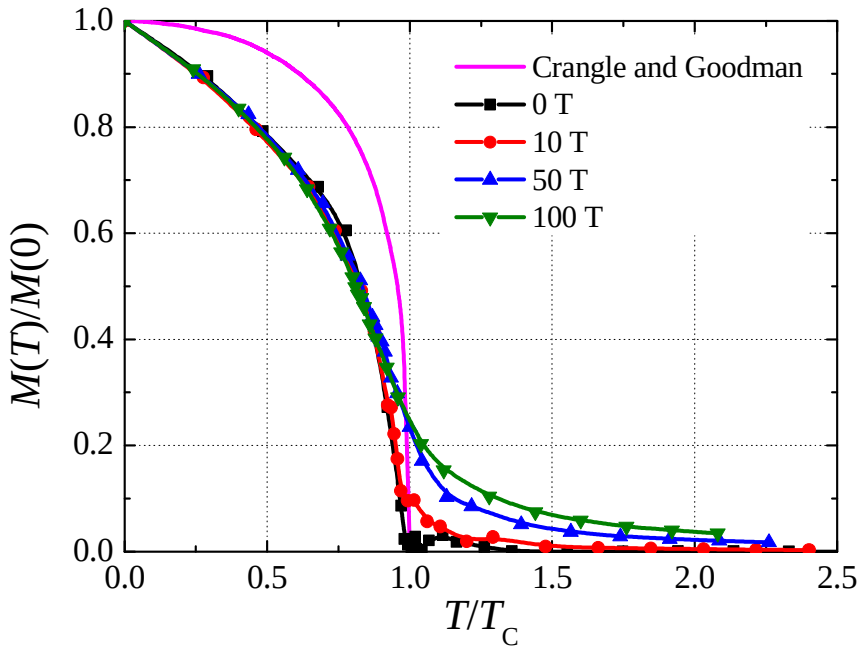

Fig. 4.2 – Reduced magnetization against T/T_C showing the beginning of the abrupt change near the critical region at $T = 0.9T_C$. The experimental result comes from Ref. [6]. A more abrupt variation of reduced magnetization occurs near the transition temperature regime, justifying the location of the transition temperature by the inflexion points.

(ii) Atomic Magnetic Energy

Once the transition temperature can be determined from the temperature dependence of magnetization, its relation to the external field strength is to be found, from which the extent of a magnetic field to shift the transition temperature can be understood, using the ground state magnetic energy.

According to Hamiltonian of the SLD system in Eq. (2.17), the atomic magnetic energy at ground state with an external field, $E_{0\mathrm{K}}^{\mathrm{mag}}$, is written as

$$E_{0K}^{\mathrm{mag}}\left(\boldsymbol{H}^{\mathrm{ext}}\right) = -\frac{1}{2N}\sum_{i,j} j_{ij} - g\mu_{\mathrm{B}} S\left|\boldsymbol{H}^{\mathrm{ext}}\right|, \tag{4.7}$$

where N is the number of atoms in a magnetic system, and the direction of $\boldsymbol{H}^{\mathrm{ext}}$ is opposite to that of $\boldsymbol{S}$. In Eq. (4.7), the term $-\frac{1}{2N}\sum_{i,j} j_{ij}$ represents the ground state atomic magnetic energy per atom, and is found to be about -0.175 eV from SLD simulation using CDD potential [[8]]. Fig. 4.3 shows the simulated value of $E_{0\mathrm{K}}^{\mathrm{mag}}$ for various $\left|\boldsymbol{H}^{\mathrm{ext}}\right|$ attempted in SLD simulations. It can be seen from Fig. 4.3 that $E_{0\mathrm{K}}^{\mathrm{mag}}$ is linearly dependent on $\left|\boldsymbol{H}^{\mathrm{ext}}\right|$, as expected in Eq. (4.7).

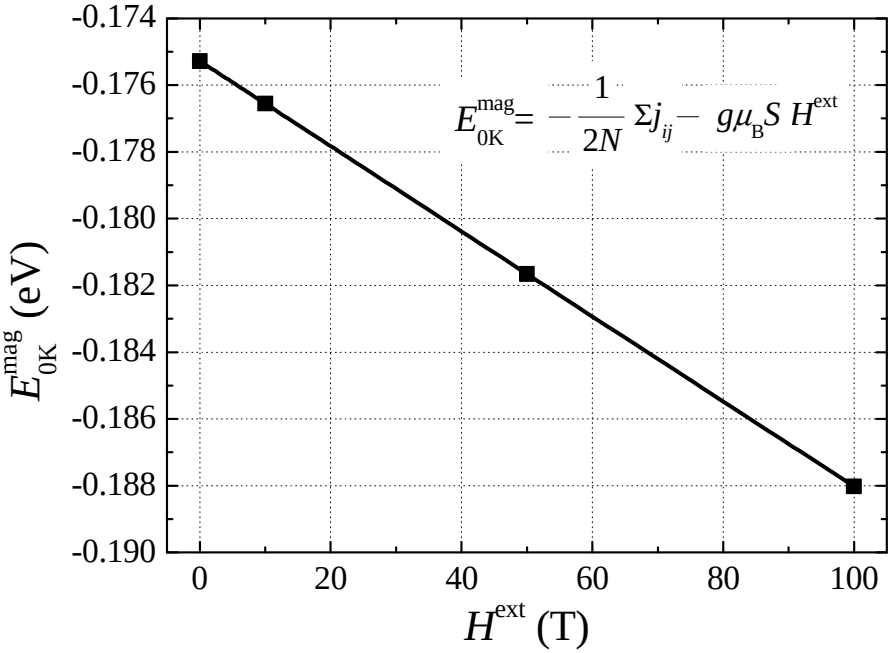

Fig. 4.3 – Ground state magnetic energy against field strength according to Eq. (4.7), showing a linear relationship between these two quantities.

Following the location of the inflexion points for various field strengths shown in Fig. 4.1, it is possible to speculate a linear relationship between the external field and the transition temperature by

$$-E_{0K}^{mag} = \gamma k_B T_C , \tag{4.8}$$

where γ is a proportionality constant to be estimated that connects E_{0K}^{mag} and T_C. Combining Eq. (4.7) and (4.8), we have

$$\begin{aligned} \gamma k_B T_C &= -\left\{ -\frac{1}{2N}\sum_{i,j} j_{ij} - g\mu_B \left| \boldsymbol{H}^{ext} \right| S \right\} \\ &= \frac{1}{2N}\sum_{i,j} j_{ij} + g\mu_B \left| \boldsymbol{H}^{ext} \right| S \end{aligned} , \tag{4.9}$$

from which we may further reduce it to

$$T_{\mathrm{C}} = P' + Q' \left| \boldsymbol{H}^{\mathrm{ext}} \right|, \tag{4.10}$$

where $P' = \frac{1}{\gamma k_{\mathrm{B}}} \frac{1}{2N} \sum_{i,j} j_{ij}$ and $Q' = \frac{1}{\gamma k_{\mathrm{B}}} g \mu_{\mathrm{B}} S$ are the intercept and the slope of the linear equation in Eq. (4.10), respectively. After linear fitting for P' and Q' by means of the observed T_{C}'s and the applied fields, γ is found to be around 2.00 from both P' and Q'. Fig. 4.4 shows the fitting results, and verifies the linearity speculation, which is reasonable because the ground state magnetic energy in Fig. 4.2 also varies linearly with applied field strength. It is thus possible to suggest that $\gamma \approx 2.00$ could demonstrate the linear relation between $\left| \boldsymbol{H}^{\mathrm{ext}} \right|$ and T_{C}. The proportionality constant $\gamma \approx 2.00$ is larger from the quantum mechanical calculation of 1.5 for the zero-field case (See Eq. (4.4)), which should result from the absence of spin correlation along *x* and *y* components in MFT calculations.

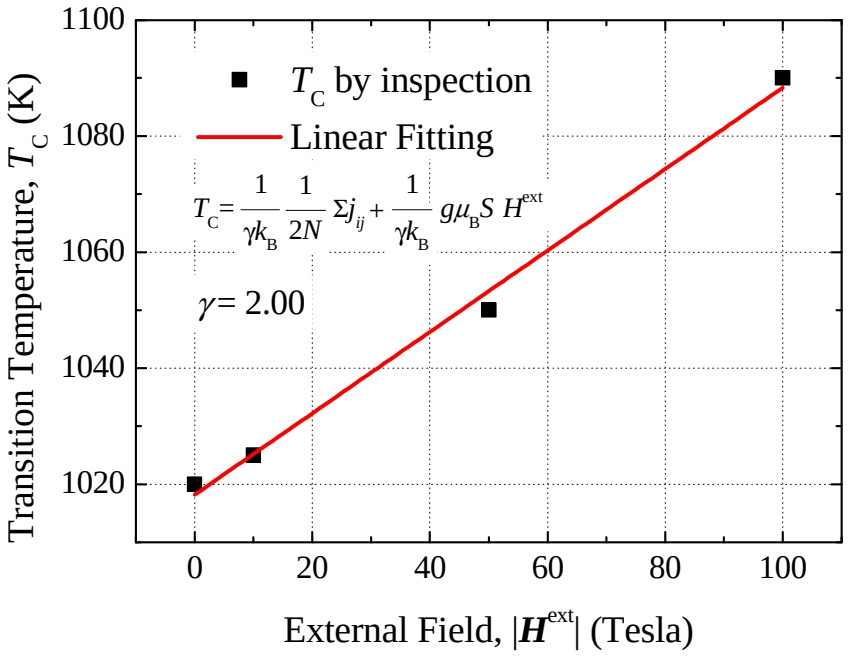

Fig. 4.4 – Linear external field dependence of the transition temperature. The choice of $\gamma = 2.00$ is suggested according to Eq. (4.9), with the straight line showing the fitting results for $\gamma = 2.00$.

(iii) Reduced Magnetization

Since SLD is already known for accurately estimating the zero-field Curie temperature by considering the correlation of *x* and *y* spin components, as opposed to MFT, it is interesting to further realize the extent of an external field for MFT to emulate SLD.

The MFT reduced magnetization in Eq. (4.5) is used as an indicator of the deviation between MFT and SLD. Note that the lattice constants *a* used in Eq. (4.6) to obtain Eq. (4.5) come from SLD simulations at elevated temperatures and field strengths. It is noticed that the calculation results of the reduced magnetization from SLD are departed from the predictions of MFT, as shown in

Fig. 4.5. It is seen that the inflexion points of magnetizations calculated from SLD simulations occurs at a lower temperature than the predictions of MFT. In addition, the Curie temperature of the zero-field BCC iron found by SLD (1020 K) is closer to the experimental value of 1043 K than the MFT result with thermal expansion does (1250 K). Accordingly, at least for the external field strengths considered, MFT provides an underestimate of the abruptly decreasing trend of magnetization, such that generally a higher temperature is required by MFT to result in the magnetization value that SLD approach already achieves at a lower temperature. This happens probably because in MFT there is no correlation between *x* and *y* components of a spin vector, which is involved in the three dimensional Heisenberg model used in our SLD calculations. In another perspective, one may realize that a strong magnetic field allows the reduced magnetization from SLD to approach that from the MFT closer by comparing the dots and lines belonging to that field strength, because the external field contribution to the total effective field becomes more significant than the *x* and *y* spin components. This interpretation confirms the insignificance of the spin correlation along *x* and *y* components in MFT.

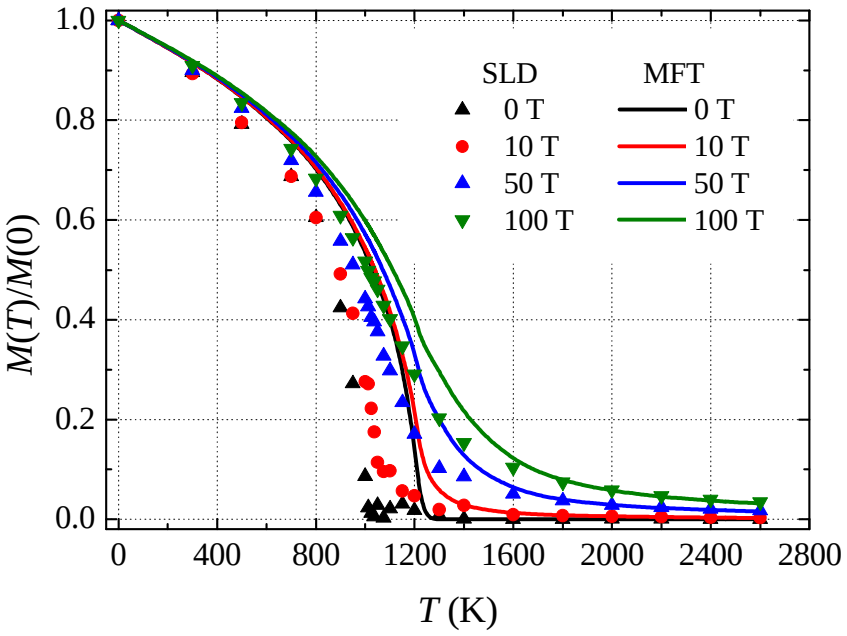

Fig. 4.5 – Temperature dependence of reduced magnetization from both SLD and MFT at varying volume. Dots represent the SLD results, whereas the lines represent the MFT results. The MFT generally results in a higher transition temperature than SLD does, probably due to the negligence of the correlation along the precession components in MFT.

Even though the SLD results are departed from the MFT one, it is possible to define a scale for describing the effect due to correlations with x and y components, such that the calculated results of magnetization by MFT can be consistent with the corresponding SLD results in Fig. 4.1. This idea can be realized by adjusting the scale of the effective field used in the mean field theory, such that

$$H^{\text{eff}} = A\left(\frac{e^{z}}{g\mu_{\text{B}}}\sum_{i} J_{ij} - H_{z}^{\text{ext}}\right), \tag{4.11}$$

where A is the scaling factor, and put this scaled effective field in the MFT equation in Eq. (4.5) for iteration.

The scaling factor A could be determined by fitting the scaled MFT results to those found by SLD, such that the mean field magnetization curves show little discrepancy with the SLD simulation results. The scaling factors in Table 4.1 rely on three methods as the convergence criteria: (a) most approximate integration area under curve, (b) least algebraic sum of residuals, and (c) least squared sum of residuals. Here, the residual refers to the difference between iterated MFT magnetization and the SLD magnetization. The values of the scale factor show that A increases with the external field strengths attempted here for all three convergence criteria, and the field strength dependence of the scaling factor indicates the increasing resemblance of MFT to SLD under strong fields, in which case the uncorrelated portion of the effective field dominates the molecular field. The fact that $A \leq 1$ implies that the mean field should reduce its effect on the *z*-component and instead make more contribution to the *x* and *y* spin components, in order to make MFT more consistent to SLD.

Table 4.1 – Scaling factor *A* of the effective field in the mean field theory to match the SLD results in different convergence criteria.

Field (Tesla)	0	10	50	100
A (approximate area)	0.81801	0.84303	0.89546	0.92311
A (algebraic residual)	0.81855	0.84271	0.88856	0.91114
A (squared residual)	0.81805	0.83801	0.88477	0.90609

If the scaling factors are plotted against the external field strength, as is done in Fig. 4.6, one can determine the scaling factor at any field strength between 0 T and 100 T along the curves, such that MFT can emulate SLD. All three methods return similar scaling factors. It should be noted from Fig. 4.6 that the scaling factor is associated with the strength of external field. It is also reasonable to expect that an external field much greater than 100 T is needed to let the MFT results conform to the SLD one, such that A equals 1, at which condition the spin-uncorrelated part of the effective field contributes most.

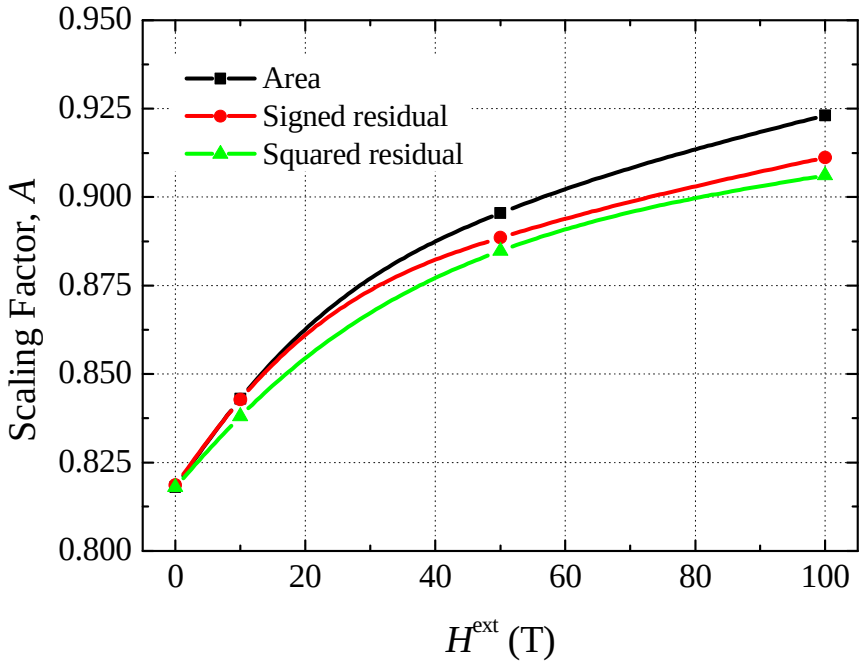

Fig. 4.6 – Scaling factor of the effective field in MFT to resemble the SLD results, as shown in Eq. (4.11). A larger value of the scaling factor is needed for a stronger external field, such that the SLD results resemble the MFT counterpart without considering precession.

Fig. 4.7 shows the fitting results for each scaling factor used in Table 4.1 graphically, with those three fitting criteria mentioned above, showing that the fitting is satisfactory over the temperature range attempted regardless of the field

strengths applied, and supporting the idea that the disagreement in normalized magnetization between SLD and MFT could be modeled by an external-field-dependent scaling factor.

From the above discussion, the scale factor A can be loosely regarded as the proportion of the mean field that should be contributed to the external field direction, whereas $(1-A)$ can be treated as the mean field responsible for spin precession. By introducing A, the MFT can resemble SLD.

In summary, the external magnetic field maintains the long range magnetic ordering, especially beyond the transition temperature. Also, this section has suggested an empirical relation to determine the transition temperature from the ground state magnetic energy and the external field, and has compared SLD magnetization with the MFT counterpart, addressing the importance of considering spin correlations in an atomistic simulation method to model zero-field or field-induced magnetization more pertinently to meet experimental results.

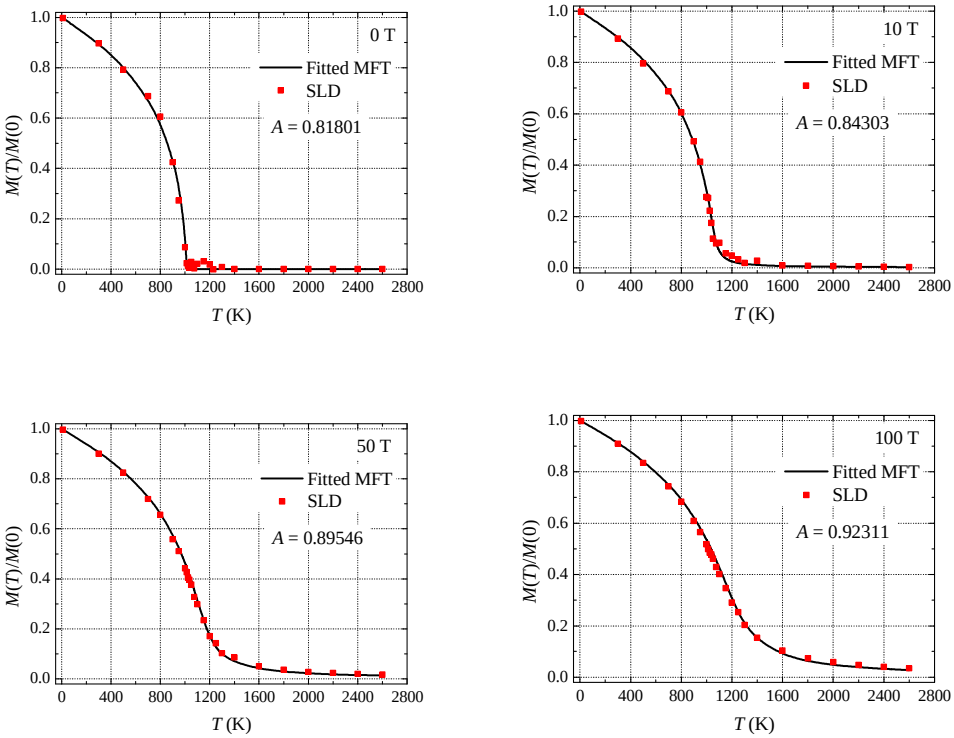
0 T
Fitted MFT
SLD
A = 0.81801
10 T
A = 0.84303
50 T
A = 0.89546
100 T
A = 0.92311
M(T)/M(0)
T (K)

Fig. 4.7 (a)

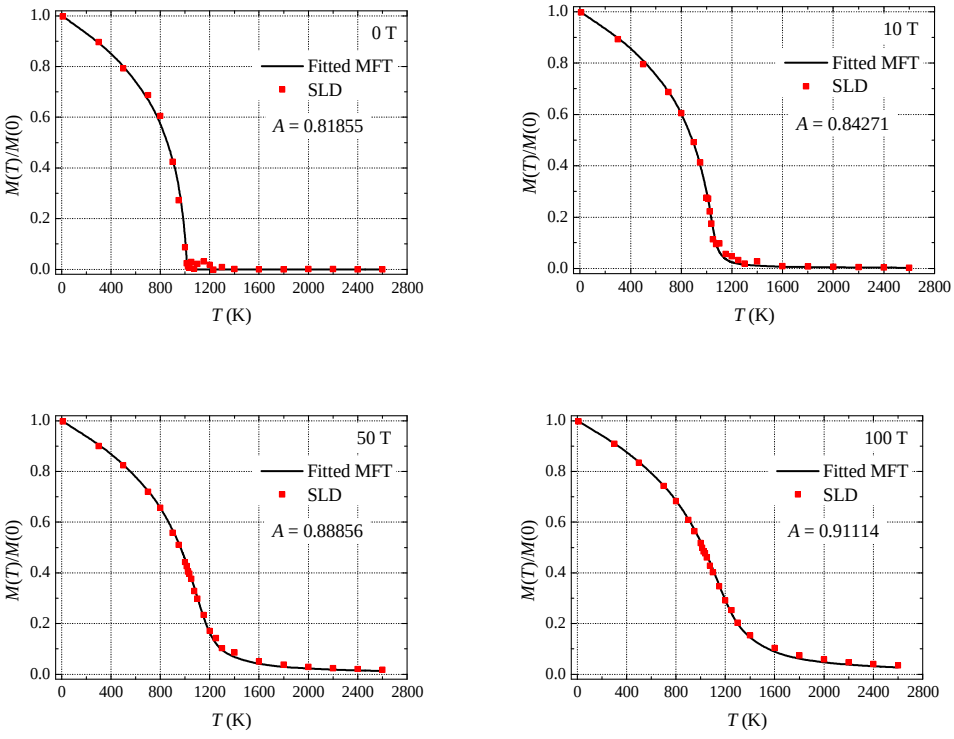
0 T
Fitted MFT
SLD
A = 0.81855
10 T
A = 0.84271
50 T
A = 0.88856
100 T
A = 0.91114
M(T)/M(0)
T (K)

Fig. 4.7 (b)

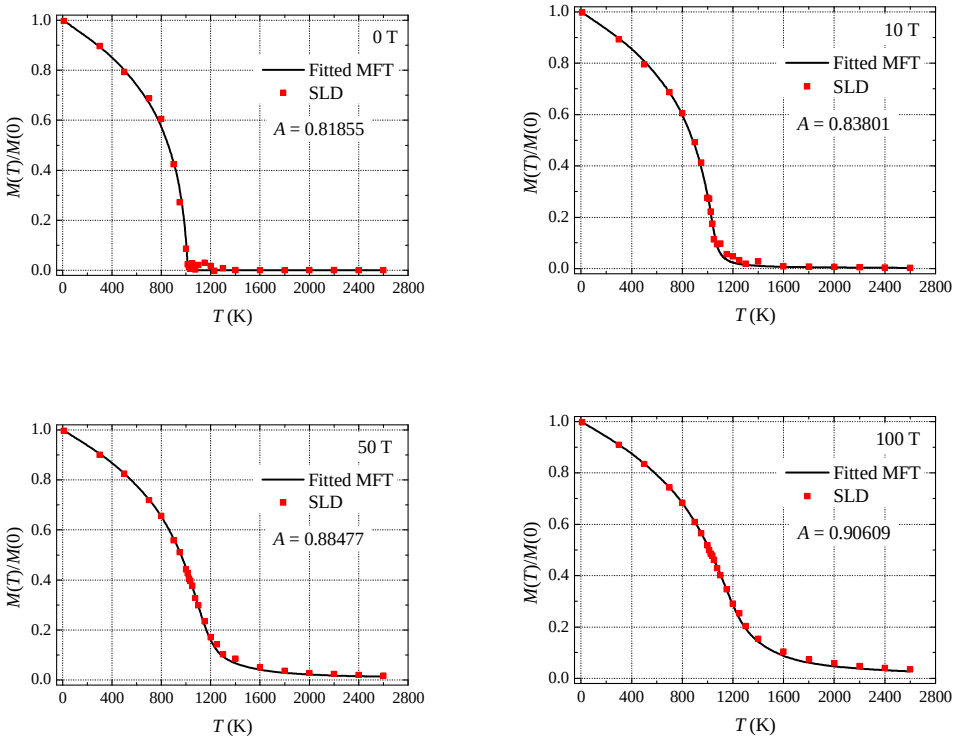

Fig. 4.7 (c)

Fig. 4.7 – Individual fitted results of the scaled effective field in MFT, compared with SLD, in (a) approximate area approach, (b) algebraic residual approach, and (c) squared residual approach, respectively.

2. Short Range Magnetic Ordering

Short range magnetic ordering, similar to the long range counterpart, is another perspective resulting from the classical spins. Two quantities can reflect the short range ordering: spin correlation functions and the effective magnetic field strength, because they depend on the neighboring spins but not on all spins in a given bulk.

The spin correlation function $\boldsymbol{e}_i \cdot \boldsymbol{e}_j$ acts as an indicator of short range magnetic ordering, from which their dependence on temperature and field strength can be noticed. It is expected that the external field effect on the short range ordering exhibits a similar trend as the long range counterpart because short range orderings also come from spin collinearity, which can be controlled by an external field. Fig. 4.8 (a) and (b) shows the ensemble average of the spin-spin correlation functions, $\left\langle \boldsymbol{e}_i \cdot \boldsymbol{e}_j \right\rangle$, due to the first and second nearest neighbors of BCC Fe atoms, respectively. The graphs show that the external field maintains the spin-spin correlations, just as it maintains the atomic magnetization, and that the applied field increases the transition temperature determined by the inflexion points, whose values are similar to those from Fig. 4.1. The agreement of the transition temperatures in these two graphs indicates the consistency of long-range and short-range magnetic ordering in reflecting the temperature dependence of magnetic behavior. The non-zero values of the correlation functions far beyond the transition temperature indicate the existence of short range ordering that can hardly be removed completely by thermal excitations.

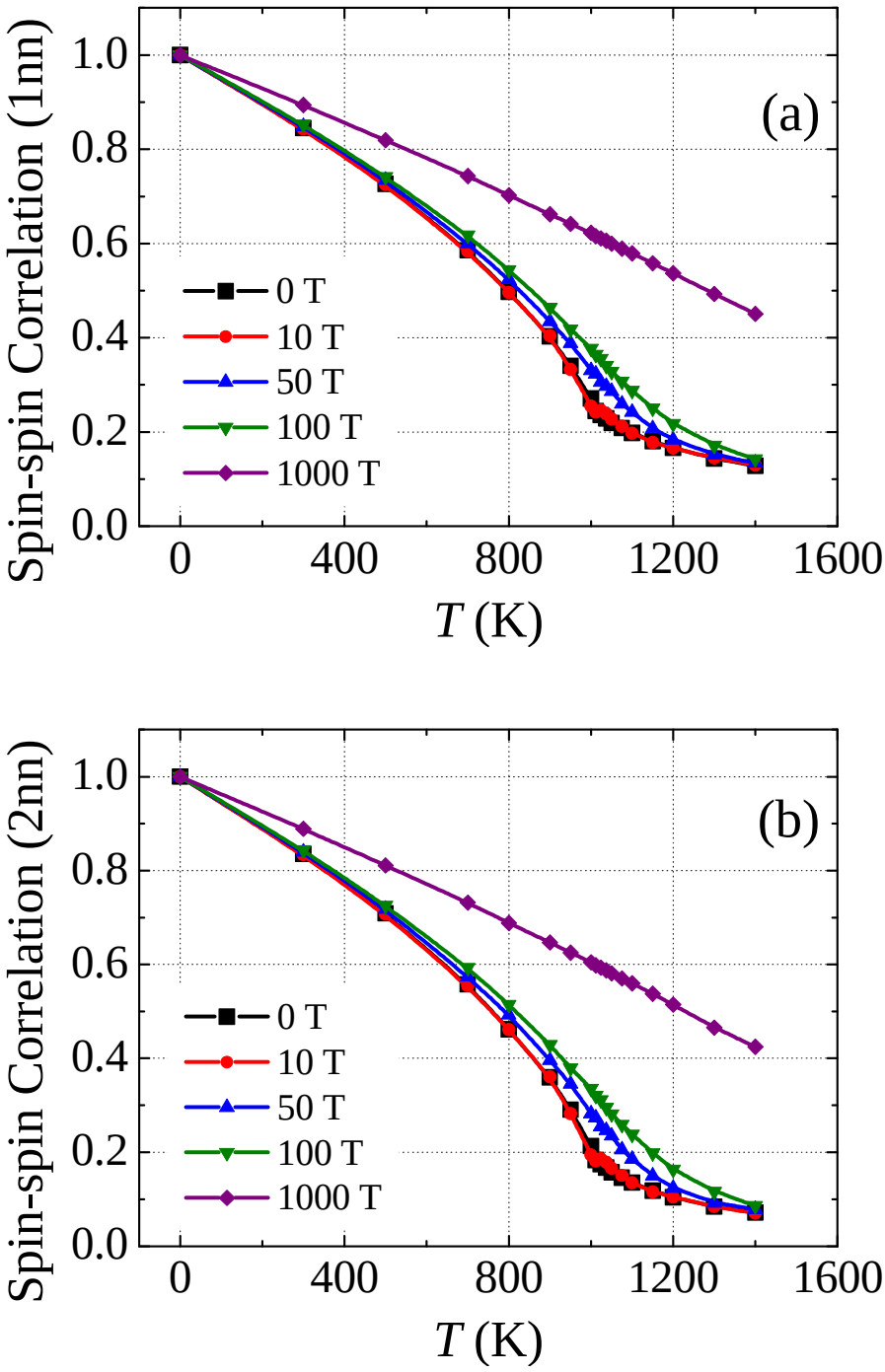

Fig. 4.8 – Spin-spin correlation function of BCC Fe within (a) the first nearest neighbors (1nn) and (b) the second nearest neighbors (2nn) against temperature under various magnetic fields tried. Both graphs can indicate the increase in the transition temperature with the applied field as the temperature dependence of magnetization does.

The total effective magnetic field is also characteristic of the short-range magnetic ordering because it depends on the spin orientation of the nearest neighbor spins. In fact, it can be shown that the effective magnetic field has the same purpose on spin dynamics as the force constant does on lattice dynamics. Note that the atomic spin motion has the form

$$\frac{d\boldsymbol{S}_i}{dt} = \frac{1}{\hbar}\boldsymbol{S}_i \times g\mu_{\mathrm{B}}\boldsymbol{H}_i^{\mathrm{eff}}, \tag{4.12}$$

and the lattice motion has the form

$$\frac{d\boldsymbol{p}_i}{dt} = -k_i\boldsymbol{r}_i, \tag{4.13}$$

where k_i is the force constant of atom i. By comparison with these two equations, the effective magnetic field can be treated as an operator on the spin that governs the spin stiffness, just as the force constant can be treated as an operator on the displacement that governs the lattice elasticity.

For an understanding of the external field effect on the effective field, Fig. 4.9 is prepared to show the temperature dependence of the *z*-component of effective magnetic field H_z^{eff} in eV along the *z*-axis, which is the direction of the applied field. From this graph, the atomic effective field can be strengthened by the applied magnetic field, which gives the minimum free energy after its alignment with spins. On the other hand, the transition temperatures found on this graph, recognized again by the inflexion points, have comparable values to those found from Figs. 4.1 and 4.8, suggesting that the external field shifts up the transition temperature, in response to the decrease of short range magnetic

ordering. From Fig. 4.9, it is possible to observe the converging trend of the effective field strength to around 0.08 eV at sufficiently high temperature, showing that the short range ordering cannot be removed completely by thermal excitation, as is already found in Fig. 4.8, even if the temperature is far beyond the transition temperature determined by the inflexion points.

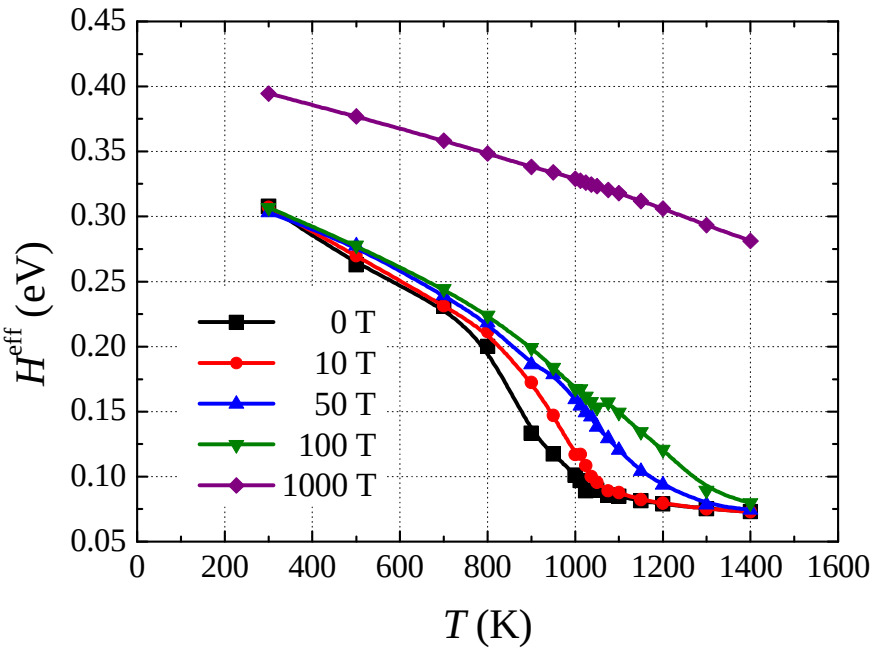

Fig. 4.9 – *z*-component of average atomic effective magnetic field at elevated temperatures, which reflects similar temperature dependence as the long range ordering does.

It can be realized that the applied external field has little contribution to the effective magnetic field, which can be understood in the following explanation. Considering the definition of the effective field,

$$\boldsymbol{H}_i^{\text{eff}} = \frac{1}{g\mu_{\text{B}}} \sum_j J_{ij} \boldsymbol{S}_j - \boldsymbol{H}^{\text{ext}}, \tag{4.14}$$

the quantity is composed of the internal magnetic field $\frac{1}{g\mu_B}\sum_j J_{ij}\boldsymbol{S}_j$, contributed by the temperature-dependent spin moment $\boldsymbol{S}_j$, and the external field $\boldsymbol{H}^{\text{ext}}$. Therefore, the resultant norm depends on both the strength of each field component and the value of the included angle between the internal and external fields. Fig. 4.10 shows schematically the vector relation.

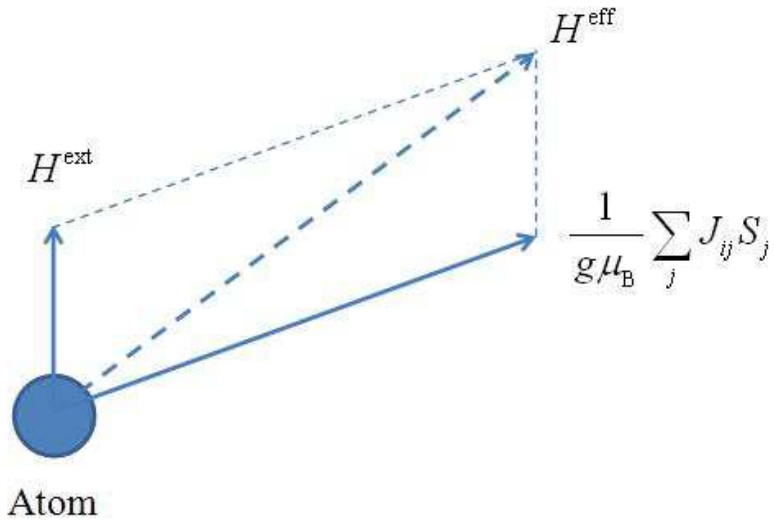

Fig. 4.10 – Vector sum of the molecular and external fields to form an effective magnetic field, showing that the external field can do little to change the norm of the effective field.

It is possible to understand how small the effect of the external field on BCC Fe is from Figs. 4.9 and 4.10, which shows the *z*-component of the atomic effective field against temperature. From this graph, the effective field components are of 10^{-1} order of eV regardless of the external field strength. Given that Table 4.2 shows H^{eff} in eV for various external fields $\left(g\mu_B S H^{\text{eff}}\right)$, together with the vector relation in Eq. (4.14), we deduce that the internal field

component $\frac{1}{g\mu_B}\sum_j J_{ij}\boldsymbol{S}_j$ should have a much larger magnitude compared to that due to the external field, regardless of the included angle size. We can recognize from Table 4.2 and Eq. (4.14) that it is only the external field component of 1000 T that is possible to change the resultant effective field vector to a larger extent. As a result, the external field generally has an insignificant contribution to spin dynamics of BCC Fe at elevated temperatures attempted, regardless of the included angle between the internal and external fields. Indeed, the internal magnetic field estimated here is already modeled by Weiss's molecular field theory, which determines the magnetic field due to spin interactions that is strong enough to achieve magnetization in the absence of an external field [9].

Table 4.2 – Norm of the external field H^{ext} in eV.

Field (T)	0	50	100	1000
H^{ext} (eV)	0	0.00636	0.0127	0.127

In summary, the external magnetic field maintains the short range magnetic ordering, but for the temperatures and fields tested it has an insignificant effect of altering the effective magnetic field.

4.3 Effects on Magnons

A magnon can be considered as a collective excitation of spins, which can be regarded as a quantized spin wave. Since it is known that the magnetic energy is changed by an external field, one may realize the effect of an external field on the magnon energy by observing the magnon properties of BCC iron.

1. Magnon Spectra

Fig. 4.11 shows 4 stacked magnon spectra at elevated external fields, keeping the temperature constant at 300 K, 800 K, 1050 K, and 1200 K, respectively.

It is observed in each graph of Fig. 4.11 that the applied field brings about the collective shift of peaks to higher frequencies, which is due to the spin hardening effect with the applied magnetic field. As the magnetic field increases, the spins further reinforce their alignment by decreasing the azimuthal angle between the spin vector and the external magnetic field, reducing the moment of inertia of the classical spins about an axis parallel to the external field. Then, the spin rotation speed increases when the moment of inertia decreases, according to the conservation of angular momentum. The spin wave thus has more energy according to the Heisenberg exchange interaction in Eq. (1.1).

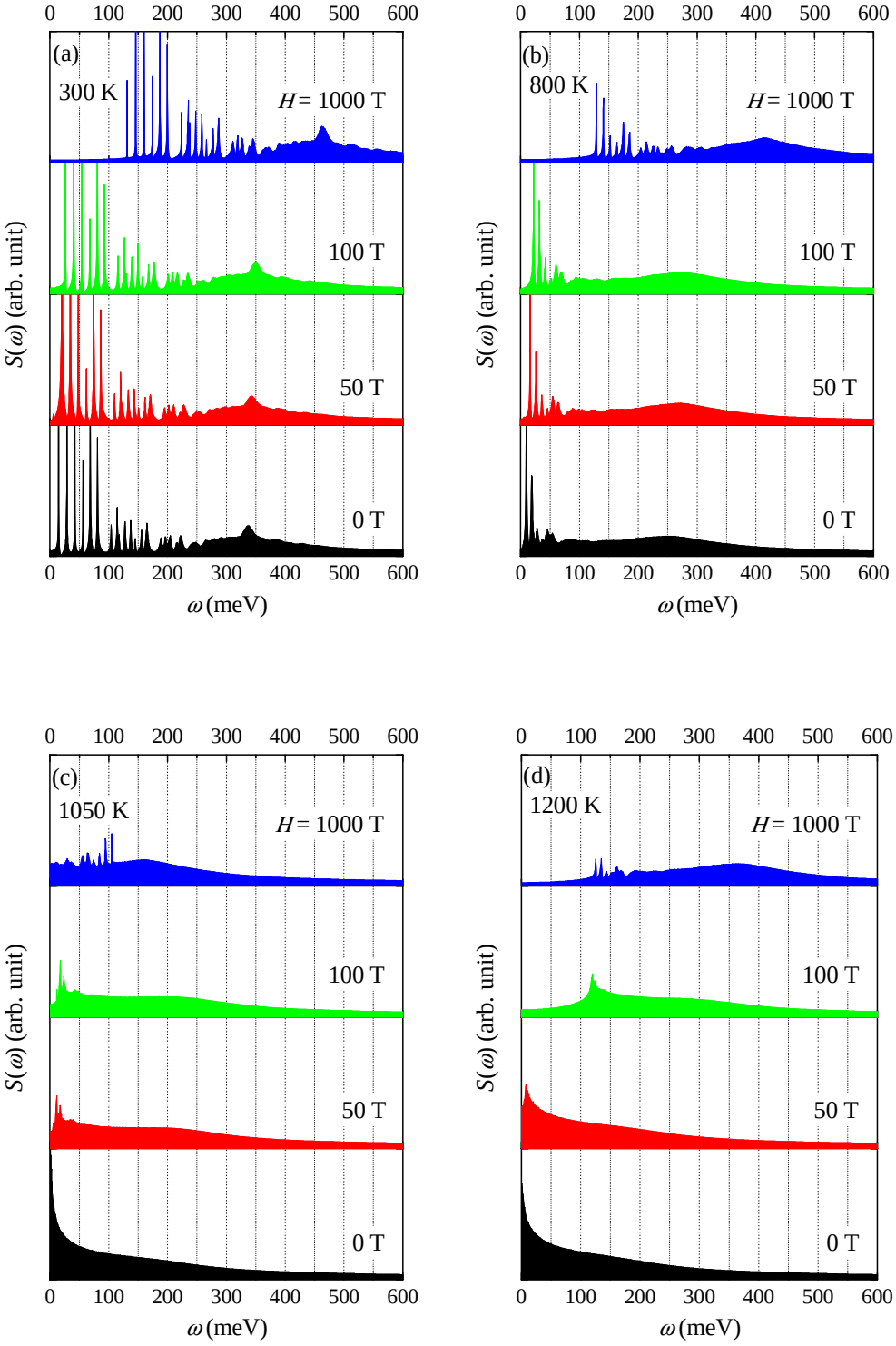

Fig. 4.11 – Mangon spectra for BCC iron at (a) 300 K, (b) 800 K, (c) 1050 K, and (d) 1200 K, respectively, under various magnetic fields. The decay of magnetic ordering can be demonstrated by the diminishing linewidth and the prominence of the low-frequency peaks.

On the other hand, the applied field slightly increases the spacing between any two successive peaks, known as the linewidth, given the same temperature. In fact, this is the evidence that an external field inhibits magnon-magnon interaction that lead to more magnon frequencies available. When the temperature is further increased while fixing the external field strength (i.e. we focus on spectra of the same color), the energy gaps are diminished due to the vigorous magnon-magnon interaction at high temperature that generates more mangons of varying frequency, leading to magnon scattering such that magnetic phase transition is identified. In fact, the collapse of the peaks at elevated temperatures can also reflect the disappearance of the long range magnetic ordering and the prominence of the remaining short range ordering.

2. Magnon Dispersion Curves

Shown in Fig. 4.12, the variation of the magnon dispersion relations with the applied magnetic field strengths are plotted at various temperatures in each sub-figure, i.e. 300 K, 900 K, 1000 K, and 1100 K, respectively. The curvature of the lines in each graph represents the spin stiffness, determined by fitting the data points with the dispersion relation for small wave-vector being

$$\hbar\omega = \Delta + Dq^2, \tag{4.15}$$

where $\hbar$ is the reduced Planck constant, ω is the magnon energy, Δ is the deviation of the magnon dispersion from zero energy value, D is the spin stiffness to be fitted, and q is the norm of the wave-vector. It is found by inspection that at a temperature below 1000 K, which is still below the magnetic

phase transition temperature of 1043 K, the applied field strength just varies the curvature of the lines indicating the spin stiffness inappreciably. However, by observing the increasing curvature of the fitted dispersion curves with increasing field at the transition temperature range (i.e. 1000 K and 1100 K for Fig. 4.12(c) and (d)), the applied magnetic field is able to realign the spins appreciably, such that magnetic ordering can be recovered and the spin stiffness is increased. It is noted that the deviation of the magnon energy points found at 1000 K and 1100 K with the fitted trend results from the difficulty locating the peak frequency from the magnon spectra of each corresponding wave-vector manually, where random error of the peak frequencies is more prominent in the magnetic phase transition boundary with greatest magnon-magnon interaction. The scattering of the magnon energy plot also indicates the disappearance of the long range magnetic ordering and the prominence of the short range ordering, as the magnon DOS can show us.

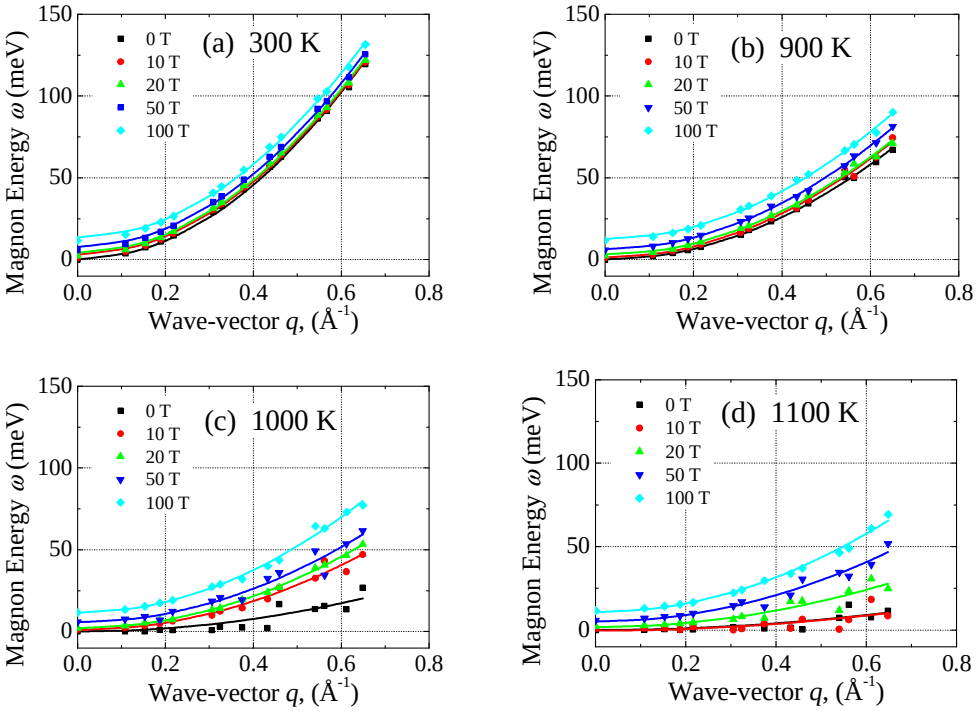

Fig. 4.12 – Magnon dispersion relations under various external magnetic field strengths, given constant temperature. Further maintenance of the magnetic ordering can be achieved by an applied field of increasing strength.

Fig. 4.13 exhibits the temperature dependence of spin stiffness D over a wide temperature range, obtained by the magnon dispersion curves such as those presented in Fig. 4.12, following the relation shown in Eq. (4.15). The deviation of the spin stiffness points with the fitted trend beyond the critical region results from the strong scattering of magnons at this temperature range. In this figure, the stiffness at room temperature is in agreement with the *ab initio* result in You *et al.* [10] of 237 $\text{meV}\,\text{Å}^2$ and Liechtenstein *et al.* [11] of 294 $\text{meV}\,\text{Å}^2$. Then the spin stiffness D generally begins with a linearly decreasing trend as temperature increases, with the value of 275 $\text{meV}\,\text{Å}^2$ at 300 K, and starts to vanish in the PM phase. The falling trend of the temperature dependence resembles those for long

and short range magnetic ordering. At temperatures far lower than the transition point found in Chapter 4.2, the external field has no appreciable contribution to the spin stiffness, as is the cases of magnetic ordering in Figs. 4.1, 4.8 and 4.9. Instead, the spin stiffness tends to converge at around 25 meV Å^2 for all field strengths attempted here. The possible reason for such a convergence value in the PM phase is that there is still short range magnetic ordering contributing to the spin waves (see Fig. 4.8 (a) and 4.8 (b)). In short, we may claim that the application of an external magnetic field is helpful to maintain the spin stiffness, especially at temperatures around the transition point. However, the maintenance is weakened beyond the transition temperature.

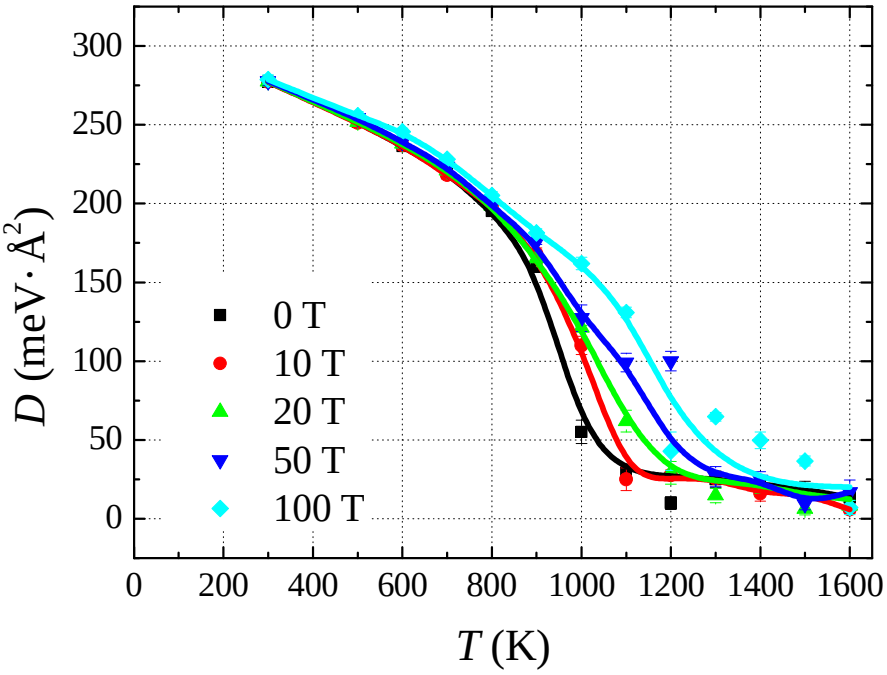

Fig. 4.13 – Spin stiffness at elevated temperatures, given constant applied field strength. The trend lines are obtained by fitting with the calculated D values. The temperature dependence of D can also be an indicator of magnetic ordering.

It can be seen from each sub-figure of Fig. 4.12 that the magnon energy at zero wave-vector, Δ, indicated by the intercept at the ordinate axes, rises with the applied magnetic fields attempted. It seems from each sub-figure that a given external magnetic field shifts up the whole set of curves, such that Δ should be more dependent on field strength than on temperature. By noting that the zero wave-vector corresponds to an infinite wavelength $\lambda \to \infty$ according to $|\boldsymbol{q}| = \frac{2\pi}{\lambda}$, which exists in an infinite bulk, we may incorporate Δ to the magnon dispersion relation in [12] to become

$$\hbar\omega = \Delta + 4JS\left(1 - \cos qa\right), \tag{4.16}$$

which returns the energy value of Δ for a zero-vector at $\boldsymbol{q} = 0$. In addition, according to the Cartesian spin wave components forming Eq. (4.16), the spin wave at $\boldsymbol{q} = 0$ would have the same phase for all time [12]. Accordingly, this field-dependent energy refers to the uniform precession mode, in which all the spins precess at the same frequency and the same phase [13-14].

Fig. 4.14 plots the uniform precession mode Δ at elevated temperatures for various field strengths. In general, the applied magnetic field can bring about a larger Δ than without its presence, as in the case of increased magnetic ordering by an external field. Since Δ simply comes from one of the spin wave components $(\boldsymbol{q} = 0)$ in a bulk, it follows that Δ also exhibits the characteristics of magnetic ordering, especially the overall trend of spin precession. At temperatures below the transition point found in Chapter 4.2, Δ drops slightly for all field strengths tested. However, a sudden decline of this energy value is

inspected starting from the critical region at about 800 K, followed by some fluctuations at even higher temperatures, suggesting that Δ can be treated as an indicator of magnetic phase transition by showing slight temperature dependence. It is noted that some negative values of this energy at 0 T should come from the fitting error, which is also the consequence of random error in locating the peak frequency in a scattered magnon spectrum after the magnetic phase transition has been reached.

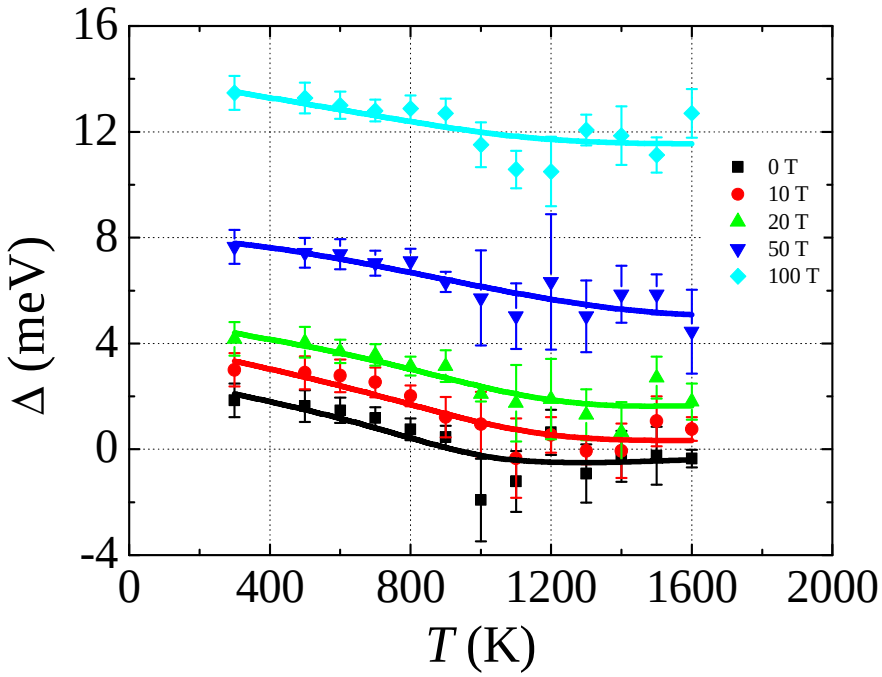

Fig. 4.14 – Uniform precession mode energy Δ at elevated temperatures, given constant applied field strength. Data points represent the simulation results, and the lines represent their predicted trends. Temperature dependence of Δ can indicate magnetic ordering as well.

Guirreiro and Rezende [15] suggested that this intercept Δ has an approximate relation to the applied field H as

$$\begin{aligned}\Delta &= E_0 = \hbar\omega \\ &= \hbar \times \frac{g\mu_B}{\hbar} \times H^{ext}, \\ &= g\mu_B H^{ext}\end{aligned} \tag{4.17}$$

according to quantum theory without considering temperature effect. By Eq. (4.17), the theoretical values of Δ at elevated applied field strengths ignoring temperature effect are those listed in Table 4.3. It is shown from the table that, below the transition point of each field, Δ obtained from the simulations seems to be about 2 meV larger than those from theory for each external field considered, but is consistent with each other at the temperature near the critical region at around 1000 K. The discrepancy of 2 meV might be due to the capability of SLD to consider temperature effects, especially before the transition point.

Table 4.3 – Theoretical uniform precession mode energy.

H^{ext} (T)	0	10	20	50	100
Δ (meV)	0	1.158	2.135	5.788	11.577

In summary, we understand that the applied magnetic field increases spin stiffness by constraining spin precession and by inhibiting magnon-magnon interactions. The spin stiffness and the uniform precession mode can also serve as the indicator of magnetic phase transition reliably.

4.4 Effects on Spin-Lattice Coupling

1. Phonon Spectra

In a magnetic system, the equations of motion in Chapter 2 suggest that the external field changes spin precession originally in the zero-field case, which in turn varies the atomic configuration by spin-lattice coupling. This section investigates the contribution of the applied field to the coupling effect, especially that revealed in the magnetic phase transition.

Fig. 4.15 shows the phonon spectra at a fixed temperature and varying magnetic field strengths, serving as a tool of visualizing collective lattice vibrations. In each graph, the external field hardly changes the phonon spectrum at a given temperature. In other words, the applied magnetic field has little use of altering lattice vibration, at least for the temperatures and field strengths tried. Indeed, this observation complies with that by other researchers. For example, a similar remark has been given by Sabiryanov and Jaswal [16] on BCC Fe, according to their numerical simulations. Also, Biegala and Ulner [17] also believe that spin-lattice coupling is hard to exhibit its effect on lattice vibration. The observation here seems to indicate that the phonon-magnon interaction in BCC Fe is insignificant, at least according to the approach of SLD simulations. However, this might happen because of the more harmonic interatomic potential used here, which fails to model the anharmonic part pertinently. The potential used in the simulations is too stiff or too harmonic, since the structural phase-transition from BCC to FCC at 1183K cannot be reproduced [18]. Excited

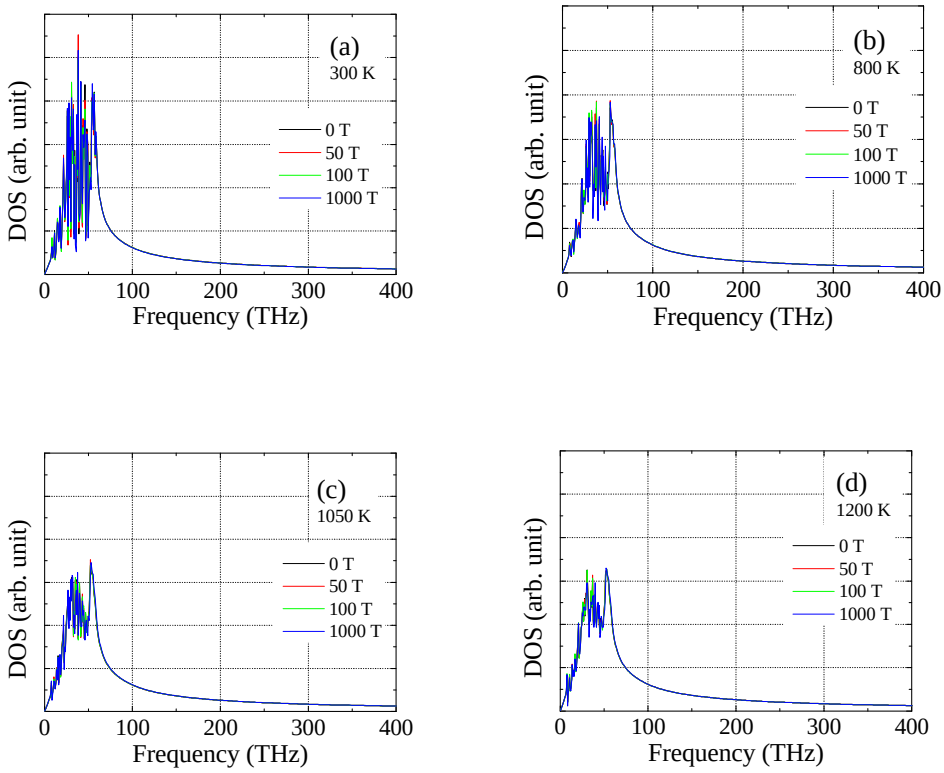

Fig. 4.15 – Phonon spectra for BCC iron at (a) 300 K, (b) 800 K, (c) 1050 K, and (d) 1200 K, respectively, under various magnetic fields from 0 T to 1000 T. The phonon spectra are almost invariant with the application of an applied field, showing that the spin-lattice coupling is limited if the current interatomic potential is used.

magnons are then too hard to interact with the phonons to change phonon vibration frequencies.

2. Vibrational energy and heat capacity

As stated in Chapter 2, the vibrational energy is related to the heat absorbed at constant volume from the ground state to the excited state, from which the heat capacity at constant volume can be derived for understanding the temperature dependence of the magnetic phase transition. Fig. 4.16 is the plot of the temperature dependence of equilibrium atomic vibrational energy for various

magnetic fields, which exhibits more appreciable anomaly around the critical region. It seems that the applied field is generally unable to alter the temperature dependence of vibrational energy, except around the critical region between 800 K and 1200 K in which a stronger field further suppresses the increase in the vibrational energy slightly. The graph confirms that spin-lattice coupling can only be found more prominently around the critical region.

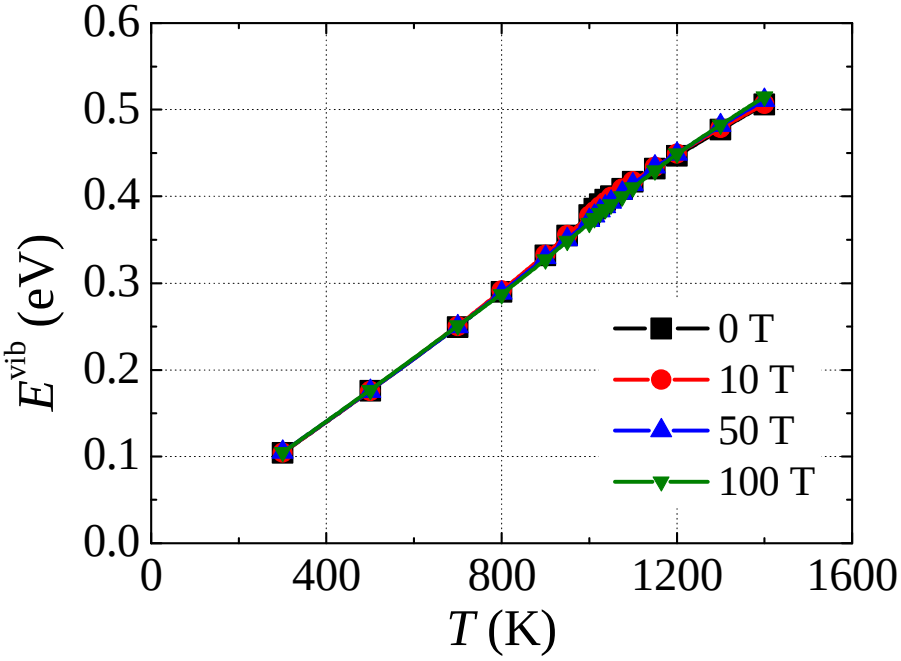

Fig. 4.16 – Ensemble average of field-induced atomic vibrational energy at elevated temperatures. The vibrational energy can exhibit magnetic phase transition around the critical region.

On the other hand, Fig. 4.17 is a plot of the heat capacity at constant pressure of zero, C_P , determined by the temperature dependence of the equilibrium vibrational energy. In fact, C_P's were evaluated as the equilibrium-volume heat capacity C_V at respective temperatures under stress-free condition $(P=0)$. Note that curve smoothing has been performed on Fig. 4.16 first for the production of

Fig. 4.17, so that a more decent trend of heat capacity can be presented from a limited number of data points shown in Fig. 4.16. Fig. 4.17 exhibits the rise of the transition temperature, located at the point of abrupt change as the magnetic field strength increases, together with the suppression of the heat capacity value with increasing field strength, so that the maximum heat capacity value decreases with the applied magnetic field strength. In addition, the transition temperatures determined by the abrupt changes in Fig. 4.17 are generally consistent with those values found in graphs describing the magnetic ordering and by the empirical relation in Eq. (4.10) with $\gamma = 2.00$. The C_P graph is attributed by the decreased entropy due to the applied field, which limits the spin orientations and hence the spin energy to be absorbed from the heat reservoir.

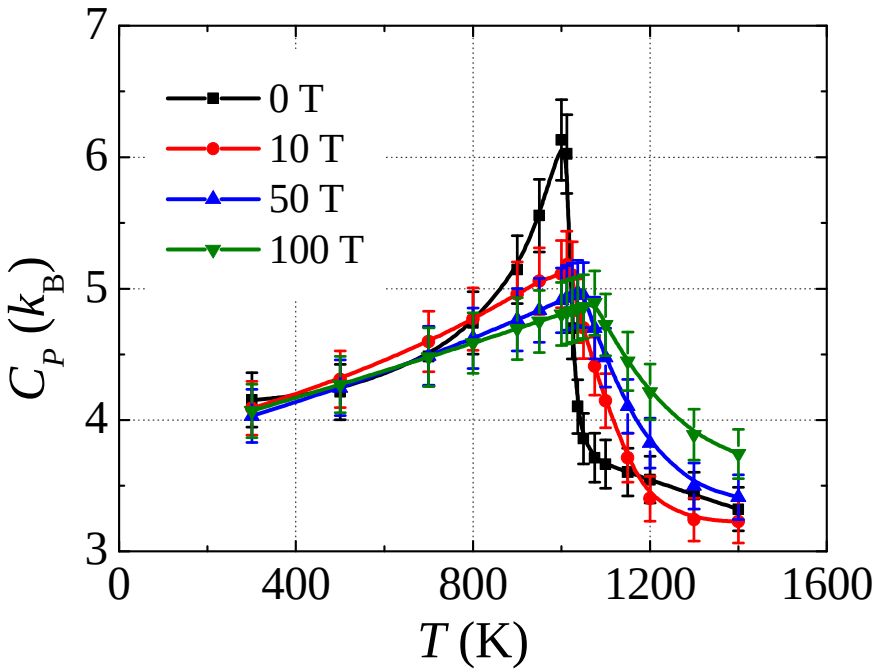

Fig. 4.17 – Fitted ensemble average of field-induced heat capacity at constant pressure of zero at elevated temperatures. This graph shows the higher shift of the transition temperature with the external field.

3. Magneto-volume Effect

Magnetic effect that alters the atomic volume is identified during thermal expansion. Fig. 4.18 shows the temperature dependence of the stress-free $(P=0)$ atomic volume under various magnetic fields, giving us an intuitive understanding of thermal expansion under magnetic fields. Note that isotropic volume change was obtained during simulation because the exchange integral J_{ij} employed in SLD is isotropic. The figure shows that the atomic volume V_{atom} increases roughly linearly with temperature despite an offset of about 11.8 Å^3 at 0 K, regardless of the applied field. The offset is near the value found in Friák *et al.* [19] and Ekman *et al.* [20], which is 11.72 Å^3 from *ab initio* calculations and 78.15 $(\text{a.u.})^3$, or 11.58 Å^3, respectively. The zero-field SLD result is able to return a Curie temperature similar to the experimental measurements of the zero-field atomic volume of BCC Fe derived from the zero-field lattice constants measured by Ridley and Stuart [21]. Accordingly, an applied field serves for suppressing the rising trend of all the curves at elevated temperatures, with a stronger field suppressing the increase in atomic volume more severely, so that the anomaly at the transition temperature is less discernible. Except the 1000 T case, such suppressions are merely more prominent between 800 K and 1300 K, but are less pronounced beyond this temperature range. In addition, this graph confirms that the phonon-magnon interaction is negligible except around the critical region, which is consistent with the experimental results.

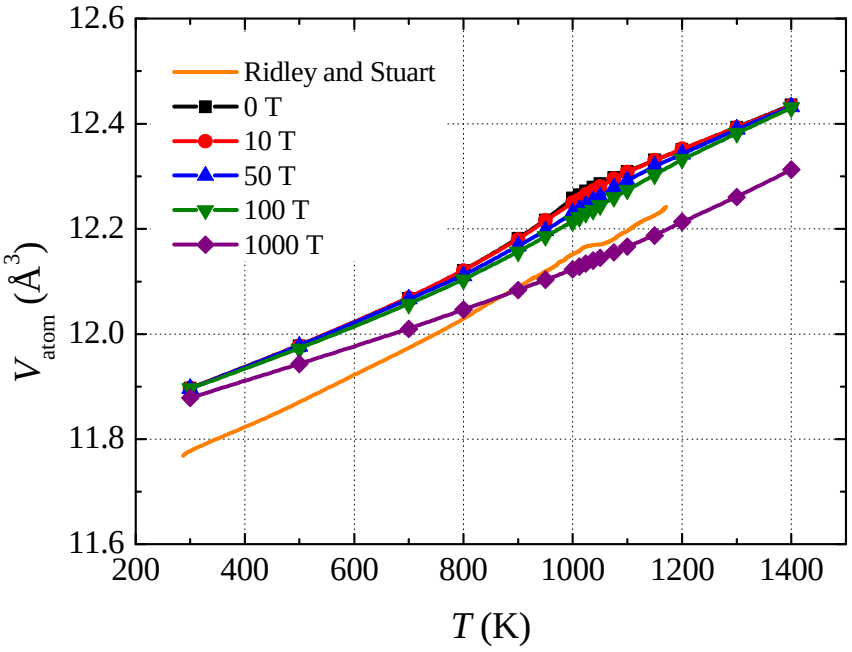

Fig. 4.18 – Temperature dependence of stress-free atomic volume of BCC iron on temperature under various magnetic fields. The experimental results derived using the lattice constants measured by Ridley and Stuart [21] in orange are used as a comparison. The SLD results can simulate the anomaly of the trend around the critical region.

Derived from Fig. 4.18, Fig. 4.19 shows the fitted volumetric thermal expansion coefficients α of BCC Fe at elevated temperatures under a number of magnetic field strengths (0 T, 10 T, 50 T, 100 T, 1000 T), so that the magneto-volume effect can be visualized more clearly. The experimental thermal expansion coefficients were derived by the thesis author, according to the atomic volume in Fig. 4.18 from Ref. [21]. Again, the number of simulated data points are far from sufficient to provide a smooth derivative of V_{atom} with respect to T, so curve smoothing is adopted on the thermal expansion coefficients here to provide a possible trend of this quantity at elevated temperatures. From the graph, one may note the similarity of the phase transition temperature from the zero-

field SLD result to that from Ref. [21], corroborating the validity of the SLD technique in estimating the transition temperature. The simulated α's for various field strengths at room temperature (300 K) are about $35\times10^{-6}\mathrm{K}^{-1}$, close to the experimentally derived value in zero-field condition by Ridley and Stuart [21]. From the graph, one can observe similar values of transition temperature to those found by magnetic ordering in Figs. 4.1, 4.8, and 4.9, all of which indicate roughly the same transition temperatures. Similar to the case of magnetic ordering, an external field hardly changes α if the temperature is below the critical region. In addition, the magnetic field increases the temperature of abrupt change and suppresses the rise of the coefficient values compared to the zero-field case, as is the case of heat capacity in Fig. 4.17. As a minor point, the rising trend of α derived from Ref. [21] after about 1,050 K is due to the corresponding rising trend of the atomic volume beyond that temperature (see Fig. 4.18). Compared to the experimental results in atomic volume and thermal expansion coefficient, it appears that the magnetic potential used in the thesis can only stress the magnetic phase transition, but lacks consideration of the condition beyond the transition.

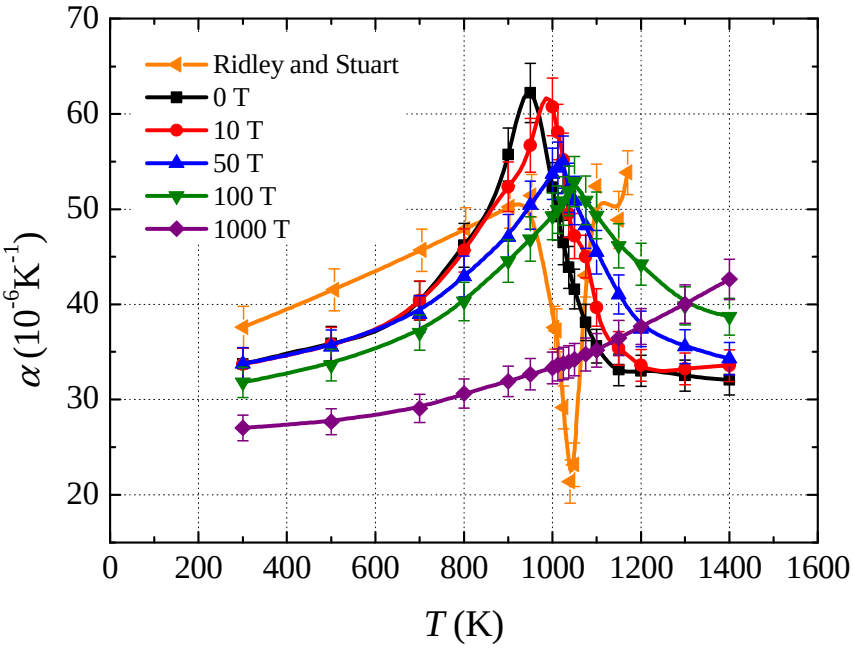

Fig. 4.19 – Temperature dependence of the fitted volumetric thermal expansion coefficient of BCC iron under various magnetic fields. The experimental results derived from [2121] were plotted in orange as a comparison. This graph can also indicate the increase in the transition temperature with the applied field.

The external field effect on the equilibrium atomic volume can be explained as follows by summarizing the previous results and discussions, in terms of both classical and quantum mechanics.

A classical explanation is given first. A magnetic field maintains the long and short magnetic ordering shown in Fig. 4.1 and 4.8, and then increases the spin precession frequency and energy, according to the spin equation of motion in Eq. (2.20). After that, the reinforced magnetic ordering comes into the momentum equation of motion in Eq. (2.19), and then decreases the magnitude of the restoring force among atoms, leading to the reduced lattice separation according to the position equation of motion in Eq. (2.18). Consequently, the

bulk shrinks. As the lattices get closer, the exchange interaction J_{ij} increases due to the increased electron wave-function overlap, and the spin orientations are maintained further. The shrinkage process will repeat in the above order, until the competition between thermal expansion and magnetic contraction is balanced to arrive at the equilibrium volume. It can be summarized that the external field changes the separation dependence of the interatomic potential, e.g. CDD potential [8] in this case, especially of the anharmonicity portion responsible for thermal expansion, such that the equilibrium separation of atoms is decreased.

A brief quantum explanation is given below. An external magnetic field inhibits magnon-magnon interactions and increases the magnon frequency, as demonstrated in the increased linewidth in Fig. 4.11. Besides, increase in magnon frequency can also be reflected by the increased spin stiffness and uniform precession mode in Fig. 4.13 and 4.14, respectively. Increase in magnon frequency further inhibits phonon-magnon interactions and hence phonon scattering, though the external field effect is only more apparent around the critical region. With inhibited phonon scattering due to the external field, thermal expansion is suppressed.

In summary, the applied magnetic field can only bring about little effect on the phonon-magnon interactions, so the resulting magneto-volume effect is not apparent except around the critical region, which can be reflected by the temperature dependence of heat capacity and thermal expansion coefficient.

4.5 References

[1] J. Hubbard, Phys. Rev. B, **19**, 2626 (1979).

[2] J. Hubbard, Phys. Rev B, **11**, 4584 (1979).

[3] J. H. Van Vleck, Rev. Mod. Phys. **17**, 27 (1945).

[4] J. S. Dyck, Č. Drašar, P. Lošťák, and C. Uher, Phys. Rev. B **71**, 115214 (2005).

[5] G. L. Zuppardo and K. G. Ramanathan, J. Opt. Soc. Am. **61**, 1607 (1971).

[6] J. Crangle and G. M. Goodman, Proc. Royal Soc. London Ser. A, Math. Phys. Sci., **321**, 477 (1971).

[7] P.-W. Ma, C. H. Woo, and S. L. Dudarev, Phys. Rev. B **78**, 024434 (2008).

[8] S. Chiesa, P. M. Derlet, and S. L. Dudarev, Phys. Rev. B **79**, 214109 (2009).

[9] S. Chikazumi, *Physics of Ferromagnetism, 2nd. ed.* (Oxford University Press, New York, 1997), p. 118.

[10] M. V. You, V. Heine, A. J. Holden, and P. J. Lin-Chung, Phys. Rev. Lett. **44**, 1282 (1980).

[11] A. I. Liechtenstein, M. I. Katsnelson, and V. A. Gubanov, J. Phys. F: Met. Phys. **14**, L125 (1984).

[12] C. Kittel, *Introduction to Solid State Physics, 8th ed.* (Wiley, New York, 2005), p. 332.

[13] R. M. Damon and J. R. Eshbach, J. Phys. Chem. Solids **19**, 308 (1961).

[14] D. D. Stancil and A. Prabhakar, *Spin Waves: Theory and Applications* (Springer, New York, 2009), p 144.

[15] S. C. Guerreiro and S. M. Rezende, Revista Brasileira de Física **1**, 207 (1971).

[16] R. F. Sabiryanov and S. S. Jaswal, Phys. Rev. Lett. **83**, 2062 (1999).

[17] L. Biegala and J. Ulner, Z. Phys. B: Condens. Matter **50**, 45 (1983).

[18] M. Y. Lavrentiev, D. Nguyen-Manh, and S. L. Dudarev, Phys. Rev. B **81**, 184202 (2010).

[19] M. Friák, M. Šob, and V. Vitek, Phys. Rev. B **63**, 052405 (2001).

[20] M. Ekman, B. Sadigh, K. Einarsdotter, and P. Blaha, Phys. Rev. B **58**, 5296 (1998).

[21] N. Ridley and H. Stuart, Brit. J. Appl. Phys. **1**, 1291 (1968).

Chapter 5: Summary and Conclusion

Ferromagnetic materials have shown an increasing importance in our daily lives, whose area of interest is the ferro/paramagnetic phase transitions at the transition temperature due to the exchange coupling between atomic spins. On the other hand, the external magnetic field effect of ferromagnetic materials, realized by enhancement of the magnetic ordering, has its scientific and technical value. One consequence of the application of an external field is the magneto-volume effect. However, no suitable mathematical approaches can describe the magneto-volume effect due to spin-lattice coupling achieved by a distance-dependent exchange integral, until the recent development of spin-lattice dynamics (SLD) simulation. It is the purpose of this thesis to realize the contribution of an external magnetic field on ferromagnetic iron in body-centered cubic (BCC) structure by using SLD simulation.

The background knowledge needed for understanding the external magnetic field effect has been introduced. First, statistical thermodynamics has been briefly discussed in an attempt to obtain thermodynamic properties from an ensemble of atoms. The Hamiltonian of a system of ferromagnetic iron atoms are stated, together with the equations of motions of the position, momentum and spin degrees of freedom. The SLD method follows, which involves the integration algorithm, temperature and pressure control. Parallel computing basics using graphics processing units (GPU) has been introduced, followed by the assembly and configuration of a GPU server applied to the computation

processes in the thesis for an efficient treatment of tens of thousands of atoms in simulations.

Next, simulation settings for the thesis has been mentioned, by means of the magnetic Chiesa-Derlet-Dudarev potential in the Hamiltonian. Data collection and processing steps have been discussed, including the evaluation of ensemble averages of energies and magnetization, the numerical calculations of derivatives, and the determination of thermal excitation spectra and magnon dispersion relations.

By SLD simulation of BCC iron, the effect of an external magnetic field can be analyzed in three perspectives: classical spins, magnons, and spin-lattice coupling. First, an external field reinforces both the long and short range magnetic ordering, and from such maintenance an empirical relation between the external field strength and the magnetic phase transition temperature is determined. In addition, the shortcoming of the mean field theory (MFT) in modeling spin precession can be understood by comparing the scaled MFT magnetization with the SLD counterpart. Second, an external field inhibits magnon-magnon interaction and stiffens the classical spins, whose effects are more pronounced in the critical region, according to the derived spin stiffness and the uniform precession mode. Finally, an external field can lead to the magneto-volume effect but it is only more discernible at the critical region, according to the temperature dependence of the heat capacity and of the thermal expansion coefficients. The limited magneto-volume effect observed could be attributed by the stiff interatomic potential used in the simulations. The resulting magneto-volume effect happens because the external field changes the separation

dependence of the interatomic potential, especially of the anharmonicity part, so that the atomic volume in equilibrium is reduced. Alternatively, the magneto-volume effect is attributed to the inhibited phonon-magnon interaction originated from the field-induced magnon-magnon interaction, leading to a decreased equilibrium atomic volume.

In conclusion, the thesis studies the external magnetic field effect of ferromagnetic BCC iron lattices using SLD. It is observed that an external field reinforces the magnetic ordering, and it is believed that the correlation in longitudinal spin precession is crucial for a more pertinent modeling of ferromagnetism. Besides, an external field inhibits magnon-magnon interactions that result in an increased value of spin stiffness and uniform precession mode. The inhibited magnon interactions would bring about the magneto-volume effect by means of the weak effect of phonon-magnon interactions around the critical region, though changes in the transition temperature can still be observed. The cause of the magneto-volume effect should be the change of distance dependence of the interatomic potential due to an external magnetic field.